Version August 25, 2026
Preprint typeset using LaTeX style openjournal v. 09/06/15

arXiv:2512.18076v2 [astro-ph.GA] 23 Aug 2026

PRECISION SPECTROSCOPY FOR 1.7 MILLION GALAXIES FROM SDSS-IV: IMPROVED SPECTRAL MEASUREMENTS AND CATALOGS FOR EBOSS

Owen S. Matthews Acuña*[1], Christy A. Tremonti[1], Kyle B. Westfall[2], Shea DeFour-Remy[1,3], Aleksandar M. Diamond-Stanic[4], Zach J. Lewis[1], Britt Lundgren[5], Drake Miller III[1,6], Lizhou Sha[1]

[1]Department of Astronomy, University of Wisconsin-–Madison, Madison, WI 53706, USA
[2]University of California Observatories, University of California, Santa Cruz, 1156 High Street, Santa Cruz, CA 95064, USA
[3]Steward Observatory, University of Arizona, Tucson, AZ 85719, USA
[4]Department of Physics and Astronomy, Bates College, Lewiston, ME 04240, USA
[5]Department of Physics and Astronomy, University of North Carolina Asheville, Asheville, NC 28804, USA
[6]Department of Astrophysical and Planetary Sciences, University of Colorado Boulder, Boulder, CO 80309, USA

Version August 25, 2026

ABSTRACT

The Sloan Digital Sky Survey IV DR17 Extended Baryon Oscillation Spectroscopic Survey (eBOSS) consists of 2,233,939 high-quality optical galaxy spectra obtained through 2" fibers, providing a rich spectroscopic resource for studying galaxy evolution across a broad redshift range. eBOSS was designed primarily for large-scale structure and BAO measurements and, as such, focused on galaxy redshifts, leaving much of the information contained in the spectra unexplored. In addition to the trove of spectra, the large number of repeat observations (197,521 duplicate spectra) enables evaluation of the survey's spectrophotometric quality. To unlock this potential, we introduce the eBOSS Data Analysis Pipeline (eBOSS-DAP), adapted from the MaNGA-DAP, which delivers measurements of emission-line fluxes and equivalent widths, stellar and gas kinematics, continuum spectral indices, and stellar population fits. Using the eBOSS-DAP, we successfully analyze 1,899,553 high-quality galaxy spectra below a redshift of $z < 1.12$ to produce an extensive spectroscopic catalog for the eBOSS galaxy sample. We characterize the calibration performance, quantify the reliability of the derived measurements, and release a suite of data products that fully exploit the power of the eBOSS dataset. These catalogs open the door to a new generation of studies in galaxy evolution and cosmology.

Keywords: galaxies: Emission Line Catalog, Absorption Index Catalog

1. INTRODUCTION

The era of publicly available big data, such as the first Sloan Digital Sky Survey data release (SDSS-I; D. G. York et al. 2000), has demonstrated that innovative applications of surveys beyond their intended scope can lead to significant advancements in astronomy. Initially designed to study large-scale structures, SDSS-I was quickly used to further the field of galaxy evolution studies following the release of the MPA-JHU catalog of galaxy emission lines, star formation rates, and stellar masses (J. Brinchmann et al. 2004).

The MPA-JHU catalog enabled one of the first analyses of the star formation main sequence at $z \sim 0.1$ (J. Brinchmann et al. 2004). These data were also used to study the stellar mass–metallicity relation (C. A. Tremonti et al. 2004; L. J. Kewley & S. L. Ellison 2008; B. H. Andrews & P. Martini 2013), the fundamental metallicity relation (F. Mannucci et al. 2010; S. Salim et al. 2014), the properties of Type II Active Galactic Nuclei (AGN; G. Kauffmann et al. 2004; T. M. Heckman et al. 2004; L. J. Kewley et al. 2006), and the impact of galactic environment on galaxy evolution (S. M. Weinmann et al. 2006; M. R. Blanton & J. Moustakas 2009; Y.-j. Peng et al. 2010).

The SDSS-IV Extended Baryon Oscillation Spectroscopic Survey (eBOSS; K. S. Dawson et al. 2016), a component of Sloan Digital Sky Survey IV (SDSS IV; M. R. Blanton et al. 2017), is the successor of SDSS I-III. Intending to map the Universe's structure by studying galaxies, quasi-stellar objects (QSOs), and the Lyman-alpha forest, eBOSS sports a much broader and higher redshift range than SDSS-I. eBOSS produced about 4 million spectra, providing a rich resource for studying galaxy and QSO properties at various redshifts. However, unlike the SDSS-I catalog, eBOSS has only been used for a few galaxy evolution studies to date (c.f., G. B. Zhu et al. 2015; T.-W. Lan & H. Mo 2018; C. Huang et al. 2019; A. Anand et al. 2021). One reason is the lack of a high-quality and well-documented emission line catalog. The current eBOSS emission line catalog (`spZline` files) provides only 18 emission lines and has relatively minimal documentation of the critical facets of the stellar continuum and emission line fitting routines (A. S. Bolton et al. 2012). Additionally, this catalog used empirical rather than theoretical stellar population tem-

Corresponding author: Owen S. Matthews Acuña:
matthewsacun@wisc.edu

plates (See §3.2.2) and Principal Component Analysis to fit the stellar continuum rather than stellar population modeling.

There are three primary goals in this work: 1) to provide an overview of the properties of the eBOSS galaxy sample; 2) to characterize the spectroscopic calibration of the survey; and 3) to measure and produce a catalog of emission lines, spectral indices, and stellar kinematics. eBOSS is a combination of at least seven different individual surveys, thus giving the eBOSS galaxy sample unique and complex characteristics beyond those of other comparable surveys (K. S. Dawson et al. 2013). To analyze the survey calibration, we make use of a unique facet of the eBOSS sample: duplicate spectra. eBOSS has a remarkable quantity of repeat observations of single objects, allowing us to assess the precision of the spectrophotometic calibration. Our final goal, to provide a catalog of emission lines, spectral indices, and stellar kinematics, is accomplished through the creation of the eBOSS - Data Analysis Pipeline (eBOSS-DAP). The eBOSS-DAP was built from the well-vetted algorithms developed for the Mapping Nearby Galaxies at Apache Point Observatory - Data Analysis Pipeline (MaNGA-DAP; K. B. Westfall et al. 2019; F. Belfiore et al. 2019).

An outline of the paper is as follows: In Section 2, we discuss the properties of the eBOSS galaxy sample and we quantify the survey's spectrophotometric quality. Then, in Section 3, we describe how we have adapted the MaNGA-DAP to work with eBOSS data and we outline eBOSS-DAP workflow. Next, in Section 4, we discuss the eBOSS-DAP's results and provide some figures that demonstrate the scientific potential of the data. In Section 5, we include a summary table containing recommendations regarding best practices when using the data from the eBOSS-DAP catalog. Finally, we provide a brief summary in Section 6.

The data products detailed in the paper are publicly available through the NOIRLab **Astro Data Lab** (M. J. Fitzpatrick et al. 2014; R. Nikutta et al. 2020). The source code, spectral template models, and customized emission line lists are available on GitHub. Details of the data/code access are described in Data Availability.

2. DATA

2.1. *SDSS-IV Data*

The galaxy spectra analyzed in this work are drawn from the Sloan Digital Sky Survey (D. G. York et al. 2000) Data Release 17 (SDSS DR17; Abdurro'uf et al. 2022). SDSS-I obtained imaging of $\sim 1/4$ of the sky in the *ugriz* filters (M. Fukugita et al. 1996) with a drift scan imaging camera (J. E. Gunn et al. 1998) mounted in the SDSS 2.5-m telescope (J. E. Gunn et al. 2006) at Apache Point Observatory. The *ugriz* photometry (R. Lupton et al. 2001) was used to target a variety of stars, galaxies, and quasars for follow-up spectroscopy (C. Stoughton et al. 2002).

In this work, we focus on the roughly 2 million spectra obtained as part of the SDSS-III Baryon Oscillations Spectroscopic Survey (BOSS; D. J. Eisenstein et al. 2011) and the SDSS-IV Extended Baryon Oscillation Spectroscopic Survey (eBOSS; K. S. Dawson et al. 2016). The goal of BOSS and eBOSS [1] was to map the 3D structure of the universe to measure baryon acoustic oscillations at different redshifts (c.f., D. J. Eisenstein et al. 2005). This was accomplished by targeting three different types of objects for spectroscopy based on their photometric colors: Luminous Red Galaxies (LRGs) in several different redshift slices (D. J. Eisenstein et al. 2001; B. Reid et al. 2016; A. Prakash et al. 2016); Emission Line Galaxies (ELGs) at $z \sim 0.6 - 1.1$ (A. Raichoor et al. 2017, 2021), and Quasars at $0.9 < z < 2.2$ (A. D. Myers et al. 2015). SDSS-IV also conducted two smaller programs, SPIDERS (N. Clerc et al. 2016; T. Dwelly et al. 2017) and TDSS (E. Morganson et al. 2015; C. L. MacLeod et al. 2018) which target X-ray sources and variable objects respectively.

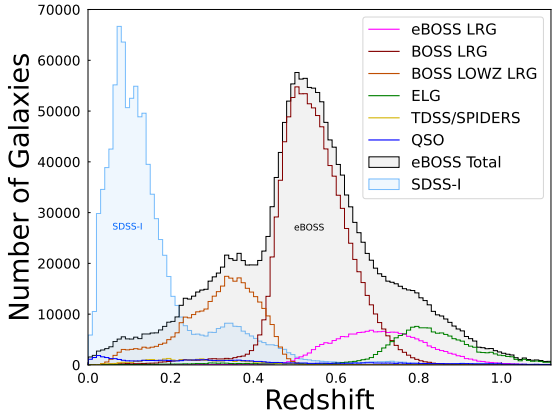


Figure 1. Redshift distribution of the SDSS-I (light blue) and eBOSS (gray) galaxy samples. The eBOSS galaxies are further divided based on how they were targeted for spectroscopy. LRGs are Luminous Red Galaxies; these galaxies are further broken down by the survey from which they originate. ELGs are Emission Line Galaxies and take up a large portion of our sample at the highest redshifts. TDSS/SPIDERS are targeted based on variable photometry and X-ray data. Finally, the histogram labeled QSO represents objects that were initially targeted as quasars but, upon further analysis, were revealed to be compact blue galaxies. In total, the eBOSS galaxy sample peaks at $z = 0.55$ and contains 1,901,834 spectra. For comparison, the SDSS-I galaxy sample contains 987,729 spectra with two peaks at $z = 0.1$ and $z = 0.35$.

Targets were observed through 2″ diameter optical fibers positioned at the SDSS telescope's focal plane using custom-drilled aluminum 'plates' that span 3 degrees on the sky. The plates enable one thousand targets (900 objects, 80 sky, 20 standard stars) to be observed simultaneously. The hole positions for fibers placed on galaxy and standard star targets were centered to account for predicted atmospheric differential refraction (A. V. Filippenko 1982). For the majority of the survey, fibers were centered to maximize throughput for 5400 Å light. However, fibers on plates targeting ELGs were centered

[1] Hereafter, we will reference the sum of both of these surveys as eBOSS.

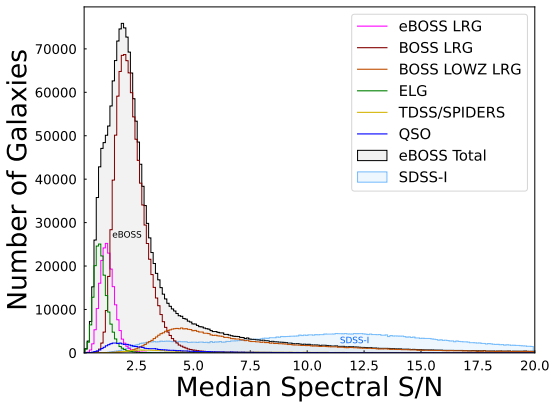


Figure 2. Median signal-to-noise (S/N) per pixel distribution of the SDSS-I (light blue) and eBOSS (gray) galaxy spectra. The eBOSS galaxies are further divided based on how they were targeted for spectroscopy. In total, the eBOSS galaxy sample peaks at S/N = 1.88. For comparison, the SDSS-I galaxy sample has two peaks at S/N = 3.9 and S/N = 12.1.

on the predicted position for 7500 Å light to maximize throughput for redshifted [OII] λ3727. In addition, some quasar targets were centered to maximize throughput at 4000Å for Lyman-alpha forest studies.

The light from the fibers was sent to the upgraded SDSS-BOSS spectrographs (S. A. Smee et al. 2013; K. S. Dawson et al. 2013), which have wavelength coverage from 3610 – 10140 Å at a spectral resolution of $R = 1560 - 2650$. Spectra were reduced by the `idlspec2D` pipeline version v5_13_2[2] (K. S. Dawson et al. 2016; S. Morrison et al. 2026). The `spectro1d` pipeline classified each eBOSS spectrum as a star, galaxy, or quasar and measured its redshift (A. S. Bolton et al. 2012).

2.2. *Sample Selection*

We selected our sample using the SDSS DR17 summary file `spAll-v5_13_2`. We chose spectra that were classified as galaxies (`CLASS = GALAXY`), resulting in 2,233,939 eBOSS galaxy spectra. The `GALAXY` class includes Type II AGN, but not Type-I (broadline) AGN (A. S. Bolton et al. 2012). We then selected only the galaxy spectra which met the SDSS survey quality standards (`PLATEQUALITY = GOOD`) and applied a redshift cut of $0.0005 < z < 1.12$ and required that no redshift warning flags were set (`ZWARNING=0`). The lower redshift limit ($\sim$ 150 km s^{-1}) eliminates some Milky Way stars that are mistakenly classified as galaxies. Our upper redshift limit was adopted because our fitting code requires either Hα or Hβ to fit the other emission lines (see §3.2.3) and Hβ redshifts out of the spectra at $z \gtrsim 1.12$. With these quality and redshift cuts, we trim the 2,233,939 eBOSS galaxy spectra to a sample of 1,901,834. Of these spectra, 197,521 are duplicates (e.g., only 1,704,313 unique galaxies were observed) with the max number of duplicates being 64 for one object .

In Figure 1, we show the redshift distribution of our galaxy spectra with the sample divided and color-coded by target class (e.g., e/BOSS LRG, ELG, QSO, etc.). We defined the target classes to encompass several broad categories by which galaxies were photometrically selected for follow-up spectroscopy (see Appendix Table A1). Details of the target selection for each object are preserved in the SDSS `spAll` file and described in K. S. Dawson et al. (2013, 2016) and references therein. The objects labeled 'QSO' were originally targeted as quasars but were spectroscopically classified as galaxies.

In Figure 2, we show the median signal-to-noise ratio (S/N) distribution of the eBOSS galaxy spectra in our sample divided and color-coded by target class. Both figures also show the distribution for the widely used SDSS-I sample. By comparing these two, we see that eBOSS is roughly two times larger with a much higher and wider redshift range while also being, on average, lower S/N than SDSS-I.

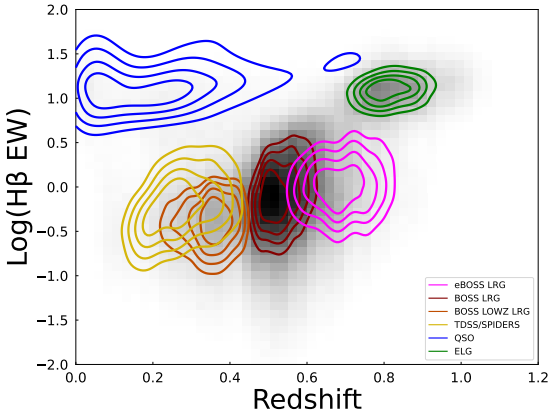


Figure 3. Hβ emission line Equivalent Width vs. redshift for all six target categories and a 2D histogram of the full sample. The target contours begin at 50% of the data.

To illustrate some of the differences between the various eBOSS target classes, we plot Hβ emission line Equivalent Width (EW) vs. redshift in Figure 3. ELGS and QSOs have much higher EWs than the LRG portion of the sample, as expected based on their color-selection. Additionally, there is a small upward trend with redshift in the LRG sample where the higher z galaxies show marginally higher Hβ EWs.

2.3. *Aperture Bias*

eBOSS observed galaxies through 2″ diameter fibers and calibrated the spectra such that their fluxes would be correct for targets that were point sources. However, the majority of eBOSS galaxies are spatially extended, leading to some aperture bias and loss of light.

To quantify this effect, we computed the fraction of the total i-band galaxy light captured by the fiber by comparing synthetic photometry computed from the spectra (found in the spAll field `spectroflux`) to the observed photometry (`modelflux`). The i-band ($\lambda_{eff} = 7480$ Å) was selected because it provides the highest S/N measurement given the red colors of most of the eBOSS galaxies. We explore trends between the fraction of light

[2] https://svn.sdss.org/public/repo/eboss/idlspec2d/tags/v5_13_2/

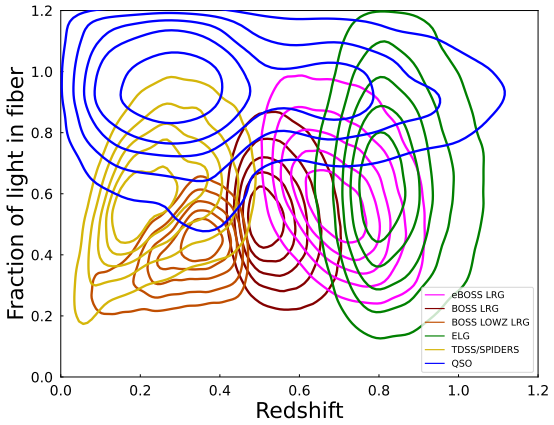


Figure 4. A two-dimensional kernel density estimate plot of the fraction of galaxy light encompassed by the SDSS fiber for the different target categories as a function of redshift. The fraction of light in the fiber is computed from the ratio of the SDSS i-band flux measured from the spectrum over that measured from photometry. This shows that different targeting categories are more likely to be fully captured by the fiber than others. The outer contours enclose 90% of the sample.

in the fiber, redshift, and galaxy target class in Figure 4. The fraction of light in the fiber ranges from $\sim 0.2-1.1$ with a median of 0.51. This is larger than the typical fraction of light in the fiber for SDSS-I galaxies (~ 0.3) since SDSS-I primarily targeted galaxies at lower redshifts ($z \lesssim 0.25$; see Fig. 1.)

Galaxies that were targeted as QSOs (blue contours in Fig. 4) have large fractions of light in the fiber since many of the quasar target selection algorithms required them to be point sources. Notably, for most other target classes, the fraction of light in the fiber increases as a function of redshift due to the smaller apparent diameter of the galaxies. Roughly 5.3% of objects have a light fraction greater than 1, implying that the spectrum is brighter than expected from the imaging data. This comes about for three reasons: i) flux calibration errors in the spectra (see §2.4); ii) errors in the photometry, which is near the magnitude limit of the survey; and iii) errors in photometric deblending which cause large galaxies to be shredded into smaller pieces, causing the fluxes from the imaging data to be underestimated (i.e., an H II region in a nearby galaxy might be categorized as a compact galaxy; see Fig.8).

In summary, for a typical eBOSS galaxy, the spectrum captures 40 - 75% of the total galaxy light. This implies that the bias due to the finite fiber aperture is not extreme; the spectra are closer to global galaxy spectra than to nuclear spectra. However, it will be essential to correct for the missing light when computing absolute quantities such as Hα-based star formation rates.

2.4. *Spectrophotometric Quality*

A major source of spectrophotometric calibration error for eBOSS — and most ground-based spectroscopic surveys — is atmospheric dispersion. Atmospheric dispersion occurs when light from celestial objects passes through the Earth's atmosphere at an angle, causing the light to refract and spread out into its component colors. The resulting image is dispersed in a direction perpendicular to the horizon by an amount that depends on the elevation of the object. At an airmass of 1.5 (elevation of 42°), light at 4000 Å and 1 μm are separated by about 1.7" (A. V. Filippenko 1982). This can affect the accuracy of spectroscopic measurements made through small apertures that can miss a fraction of the highly dispersed blue or red light.

The eBOSS data are spectrophotometrically calibrated by the SDSS `idlspec2D` pipeline as described in K. Abazajian et al. (2004) and K. S. Dawson et al. (2016). In brief, on any given plate, 20 color-selected 'standard stars' are observed. These A-to-G-type stars are not classical standards like those of J. B. Oke (1990) because their calibrated spectrum is unknown. Flux calibration is achieved by matching each star to a grid of stellar atmosphere models that have been rescaled to match the observed r-band PSF magnitude of the standard star. The use of multiple standards per plate (which are averaged with rejection) mitigates the effect of the occasional problematic star. The standard and object spectra experience approximately the same atmospheric dispersion, so, blue and red light losses are — in principle — automatically corrected by the flux calibration routine.

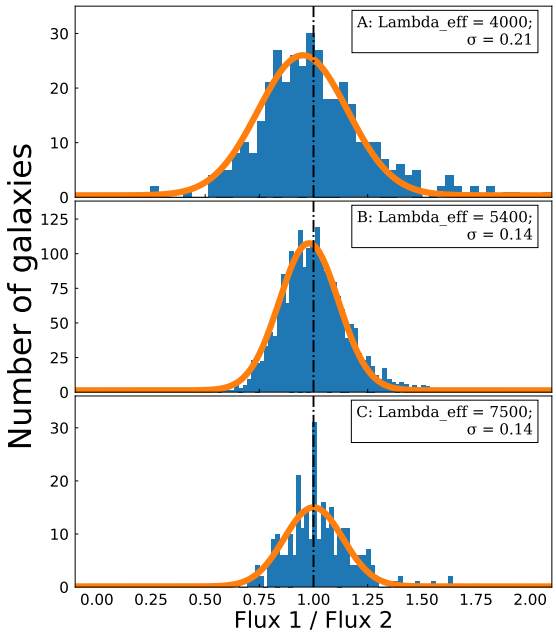


Figure 5. An estimate of the relative flux calibration error of the eBOSS spectra based on comparisons of repeat spectra of the same galaxies observed at two or more different epochs. Here we compare the sum of the flux in a 200 Å window centered at the wavelength, `LAMBDA_EFF`, that the spectrophotometric calibration is optimized for. For the majority of galaxies, this is 5400 Å (**Panel B**), however most ELG targets have `LAMBDA_EFF`=7500 Å (**Panel C**) and most QSO targets classified as galaxies have `LAMBDA_EFF` = 4000 Å (**Panel A**). The orange lines show Gaussian fits; the 1-σ spread of the data is listed in each plot. This represents the minimum uncertainty of a line flux measurement due to spectrophotometric calibration errors. These errors can be larger at wavelengths that are far from `LAMBDA_EFF` as shown in Figure 6.

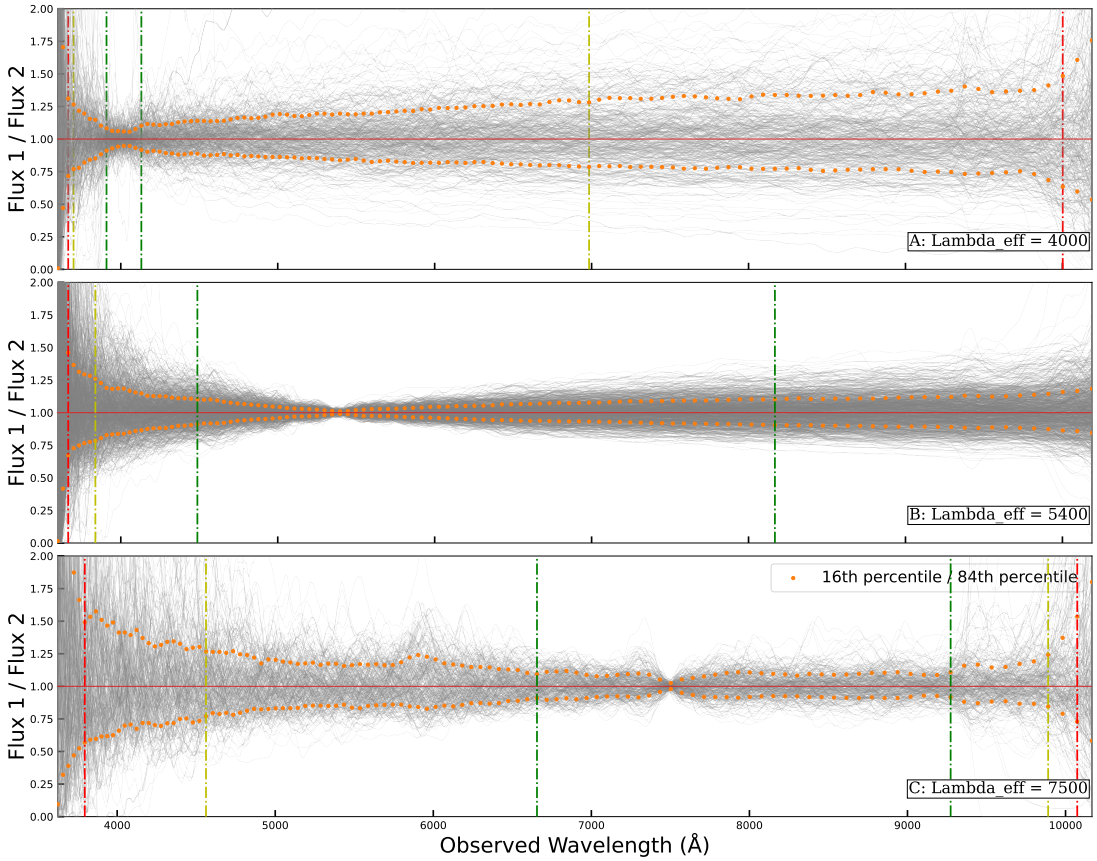


Figure 6. An analysis of the typical error in the spectral shape made by dividing pairs of repeat spectra after normalizing them at `LAMBDA_EFF`, the wavelength the flux calibration has been optimized for. We show galaxies with `LAMBDA_EFF` = 4000 Å, 5400 Å, and 7500 Å in panels A, B, and C, respectively. Each gray line represents a pair of spectra that were taken of the same galaxy in different epochs. Spectra in each pair were normalized at their respective `LAMBDA_EFF` and smoothed individually before computing their ratio. Small-scale wiggles in the gray lines are primarily due to the low S/N per pixel of the spectra. The 1σ spread of the data in 40-pixel-sized bins is shown as the orange dotted lines. Green, yellow, and red vertical lines have been added, marking where the percent error is 10%, 25%, and 50%, respectively. For most galaxies, spectrophotometric calibration errors will lead to line flux ratio errors $< 25\%$. However, caution is advised when using emission lines observed near the blue and red ends of the spectrum. For access to summary tables for this figure see Data Availability

In practice, this calibration approach works well: in the SDSS-I survey a flux calibration accuracy of $\sim 5\%$ was achieved at 4000 Å[3]. The main failure mode results from the miscentering of objects in the fibers, which can occur due to the deformation of the aluminum plug plates, which are warped to match the curved focal plane of the telescope (D. G. York et al. 2000). For example, when the hole for an object fiber is centered too high (and the majority of the standards are centered correctly in their fibers), more blue light and less red light is captured by the object fiber than for the standards, leading to an error in the relative flux calibration. The SDSS-I and II surveys used 3" diameter fibers, which mitigated the fiber centering problems. For SDSS-III/IV (BOSS and eBOSS), the fibers were reduced to 2″ in diameter to improve sky subtraction for the distant galaxies and quasars targeted. To evaluate the quality of the flux calibration in SDSS-IV/eBOSS, we take advantage of the large number of repeat galaxy spectra obtained.

In eBOSS, fibers were positioned on the plates to account for the expected atmospheric differential refraction, with different spectroscopic targets centered at different wavelengths in an attempt to mitigate light losses in particular parts of the spectrum. Most objects were centered on the position of 5400 Å light (1,716,144 spectra). However, objects targeted as QSOs were centered around 4000 Å (23,870 spectra), while objects targeted as ELGs were centered at 7500 Å (161,820 spectra). This is reflected in the parameter `LAMBDA_EFF` found in the `spAll-v5_13_2.fits` file. To analyze the relative and absolute calibration for each unique `LAMBDA_EFF`, we selected pairs of galaxy spectra after applying a cut on median S/N per pixel. For `LAMBDA_EFF` = 4000 we used a S/N >= 3 cut, resulting in 386 unique pairs. For `LAMBDA_EFF` = 5400 we used a S/N >= 6 cut, resulting in 1094 unique pairs. Finally, for `LAMBDA_EFF` = 7500 we used a S/N >= 1.5 cut, resulting in 279 unique pairs. The S/N cuts were implemented to reduce problematic negative pixels; the S/N thresholds are different for each `LAMBDA_EFF` to enable a reasonable number of pairs in each bin. In principle, these S/N cuts do not affect our analysis since the spectrophotometric quality is indepen-

[3] https://classic.sdss.org/dr7/products/spectra/spectrophotometry.php

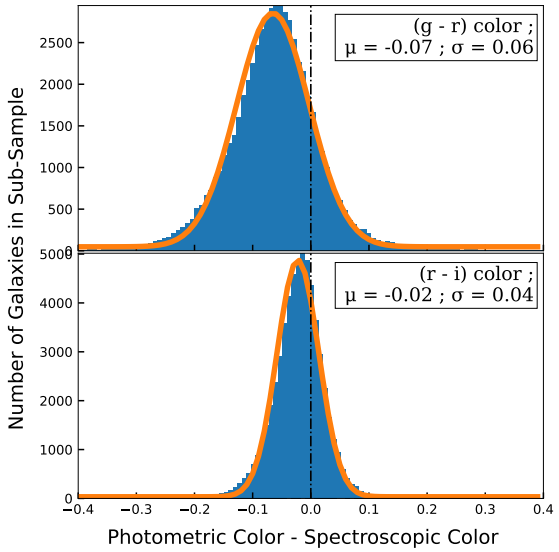


Figure 7. Comparisons of galaxy colors synthesized from the spectra with photometric colors for galaxies with $r < 17.7$ mag and spectra with LAMBDA_EFF = 5400 Å. This comparison measures the absolute calibration quality in eBOSS spectroscopy. Relatively bright galaxies are chosen for this comparison to minimize random error. In the **Top Panel**, $(g-r)$ colors are compared, whereas in the **Bottom Panel**, $(r-i)$ colors are compared. Lower σ values and μ values closer to zero indicate better absolute calibration.

dent of S/N.

In Figure 5, we show the ratios of a 200 Å flux window centered at the LAMBDA_EFF in pairs of galaxy spectra. The pairs represent spectra of the same galaxy obtained at different epochs. In some cases, the same plate was observed on multiple dates; in others, the galaxies were targeted on two different plates with different sets of standards. The ratio of the galaxy fluxes at the LAMBDA_EFF provides a valuable assessment of the repeatability of the absolute flux calibration at this wavelength. A Gaussian fit to the distribution has a width of $\sigma = 0.21, 0.14, 0.14$ for LAMBDA_EFF = 4000, 5400, and 7500, respectively. Thus, for most eBOSS galaxies, the flux calibration is accurate to about 15-20% at wavelengths near LAMBDA_EFF.

In Figure 6, we explore the relative flux calibration of the spectra as a function of observed-frame wavelength for each LAMBDA_EFF. This is the error on the spectral *shape* that would impact ratios of emission lines widely separated in wavelength. Galaxy spectra are normalized at their LAMBDA_EFF, median smoothed by 100 pixels, followed by a 40-pixel average smooth, and then divided. The orange dotted line shows the 1-σ width of the distribution of all pairs in bins of 40 pixels.

According to Fig. 6, For LAMBDA_EFF = 4000 the relative flux calibration error is less than 10% between 3909 – 4208 Å, and less than 25% between 3733 – 7449 Å. The error is over 50% at wavelengths less than 3665 or greater than 10002 Å. For LAMBDA_EFF = 5400, the relative flux calibration error is less than 10% between 4488 – 8397 Å. The error is less than 25% blueward 3838 Å and over 50% at wavelengths less than 3665 Å. Finally, for LAMBDA_EFF = 7500, the relative flux calibration error is less than 10% between 6595 – 9273 Å, and less than 25% between 4562 – 9890 Å. The error is over 50% at wavelengths less than 3830 or greater than 10074 Å. These statistics suggest caution in using emission lines observed near the edge of the spectrum.

In Figure 7, we show the difference in color between the photometry and spectroscopy for galaxies with LAMBDA_EFF = 5400 Å and an r-band AB magnitude of 17.7 or smaller. The colors of the spectra have been synthesized using the SDSS filter curves (M. Fukugita et al. 1996). We compare synthetic photometry computed from the spectra (found in the spAll field spectroflux) to the observed photometry (modelflux). For this sample, ∼27.3% of the galaxy's light falls in the 2" fiber aperture, and thus we do not expect galaxy color gradients to impact our comparison significantly. At $r < 17.7$, the photometric errors on the $g-r$ and $r-i$ colors should be minor, and, as such, any deviations between the colors of the photometry and the spectroscopy likely indicate errors in the spectrophotometric calibration. Whereas Figure 6 demonstrates the consistency of the calibration, i.e., the precision, Figure 7 shows us the absolute calibration accuracy. In Figure 7, the further left the data lies, the more blue it is relative to the photometry. The $(g-r)$ color has a larger offset ($\mu = -0.07$) and standard deviation ($\sigma = 0.06$) than the $(r-i)$ color ($\mu = -0.02$; $\sigma = 0.04$).The difference in σ between the two colors is consistent with the larger spectrophotometric errors seen at blue wavelengths in the repeat spectra comparison (Fig. 6). The slight offset in $(g-r)$ color ($\mu = -0.07$ mag) implies that there are some minor systematic issues in the calibration, as previously found for SDSS-I ($\mu_{g-r} = 0.02$ mag)[4]. A similar analysis could not be performed on LAMBDA_EFF = 4000 and 7500 spectra, as there are an insufficient number of bright galaxies available for these LAMBDA_EFF.

2.5. *Known issues with the SDSS-IV data*

There exist two caveats to our data resulting from known issues in SDSS-IV that we did not rectify. The first is that some large nearby galaxies are incorrectly deblended by the SDSS photometric pipeline, leading to incorrect photometric measurements. An example is shown in Figure 8, where an H II region has been incorrectly classified as a separate photometric object and selected for spectroscopy as a quasar target. The spectrum was subsequently classified as belonging to a galaxy; however, the galaxy's stellar mass and other properties calculated from the photometry are incorrect. These deblending problems occur frequently enough at $z < 0.1$ to produce a substantial group of outliers in the eBOSS stellar mass–metallicity relation (i.e., galaxies with high metallicity and unrealistically low stellar masses; see Fig. 23). The debending problem impacts both SDSS (R. Lupton et al. 2001) and Legacy Survey (A. Dey et al. 2019) photometry. (The latter is used for our stellar masses.) Visual

[4] https://classic.sdss.org/dr6/products/spectra/spectrophotometry.php

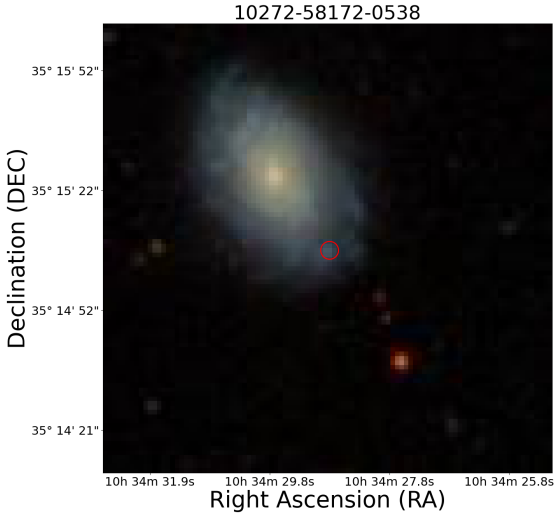


Figure 8. An example of a galaxy incorrectly deblended by the SDSS photometric pipeline. The H II region circled in red was considered a separate photometric object and targeted for spectroscopy as a quasar. (The circle represents the size of the eBOSS fiber.) The spectrum (Plate: 10272; MJD: 58172; Fiber: 0538) is classified as a galaxy and otherwise free of problems. However, quantities derived from the photometry will pertain only to the galaxy sub-region. For example, this object has a photometrically-derived stellar mass of $\log(M_*) = 5.2$ when it is clearly part of a much larger galaxy.

inspection of the Legacy Survey data shows that 5% of star-forming galaxies below $\log(M_*/M_\odot) = 7.3$ are incorrectly deblended (D. Scholte et al. 2024). Unfortunately, objects with deblending issues are not straightforward to identify without visual inspection of the photometric images. A potential approach to finding such sources would be to determine whether an object lies within the Petrosian radius of another photometric object.

Our second caveat applies to galaxies with very high emission line EWs and low gas velocity dispersions (i.e., star-bursting dwarf galaxies). In the eBOSS spectra of these galaxies, the strongest emission lines such as [O III] 5008 and Hα are sometimes clipped off. An example is shown in Figure 9. The missing portions of the emission lines typically have their inverse variance set to zero (i.e., they are flagged as bad data.) However, the lines are sometimes fit by the eBOSS-DAP if only the core of the line profile is flagged as bad; the accuracy of such fits is unclear.

The problem of clipped emission lines was well known in the SDSS-I; some code changes in DR7 improved, but did not eliminate, the issue (see §6.3 in K. N. Abazajian et al. 2009). The clipped lines arise from a combination of data reduction problems. One issue can be the saturation of the detector at the position of the brightest lines. Another issue can arise when the `spectro2D` data reduction pipeline combines the 3 - 12 individual spectroscopic exposures that make up the final spectrum. Slight mismatches between the exposures (due to small pointing differences, for example) cause the pixels associated with bright lines to be rejected because they differ by more than the errors allow between exposures.

The fully calibrated individual spectroscopic exposures are stored in the final FITS spectrum output by SDSS (the "full", not the "lite" version). Custom software for combining these exposures could likely recover many of the clipped lines. However, this is beyond the scope of the current work. In some cases, clipped emission lines can be identified by looking for discrepancies between line EWs estimated by Gaussian fits vs. straight integration (see §4.2.1) or by flagging spectra with unusual line ratios (i.e., Hα < Hβ). However, this method will not identify all cases of clipped lines, and therefore caution is advised in working with very low-mass galaxies with narrow (σ_{line} < 100 km s^{-1}) high-EW (EW> 100 Å) emission lines.

3. METHODS

We aimed to produce a catalog of emission line fits, spectral indices, and stellar population template weights from the eBOSS galaxy spectra. To this end, we developed the eBOSS-DAP, an analysis pipeline built from the Mapping Nearby Galaxies at Apache Point Observatory - Data Analysis Pipeline (MaNGA-DAP) code package (K. B. Westfall et al. 2019; F. Belfiore et al. 2019). We begin by briefly describing the MaNGA-DAP in §3.1. In §3.2 and its subsections, we describe the modifications that we made to create the eBOSS-DAP. In §3.3 we provide an overview of the eBOSS-DAP workflow.

3.1. *The MaNGA-DAP*

The MaNGA-DAP is a multi-stage spectral fitting software tool designed to process and analyze the data collected by the MaNGA survey (K. Bundy et al. 2015). It handles the complex data cubes produced by the survey, which contain spatially resolved spectroscopy of nearby galaxies. The pipeline performs various tasks, including full-spectral fitting of the galaxy spectra to measure stellar kinematics and absorption-line indices from the stellar continuum and gas kinematics, fluxes, and equivalent widths (EWs) from Gaussian modeling of the emission lines. Within the MaNGA-DAP, stellar continuum fitting is done with the Python implementation of the Penalized PiXel-Fitting method (`pPXF`; M. Cappellari 2023) using a mix of template libraries and a multiplicative polynomial. The code follows a multistage process. First, the stellar kinematics are fit with the emission lines masked. Second, the stellar continuum and emission lines are fit simultaneously, with the stellar kinematics fixed to the result of the first step. Third, the best-fit emission-line model is subtracted from the galaxy spectra before measuring the absorption-line indices. Detailed algorithms for all modules in the MaNGA-DAP are described by K. B. Westfall et al. (2019, Sections 6-10) and F. Belfiore et al. (2019, Section 2). We use Version 4.5 of the MaNGA-DAP available on Github.[5] The `examples/fit_one_spec.py` file from the MaNGA-DAP was adapted and used as the core component of the eBOSS-DAP pipeline.

[5] https://github.com/sdss/mangadap

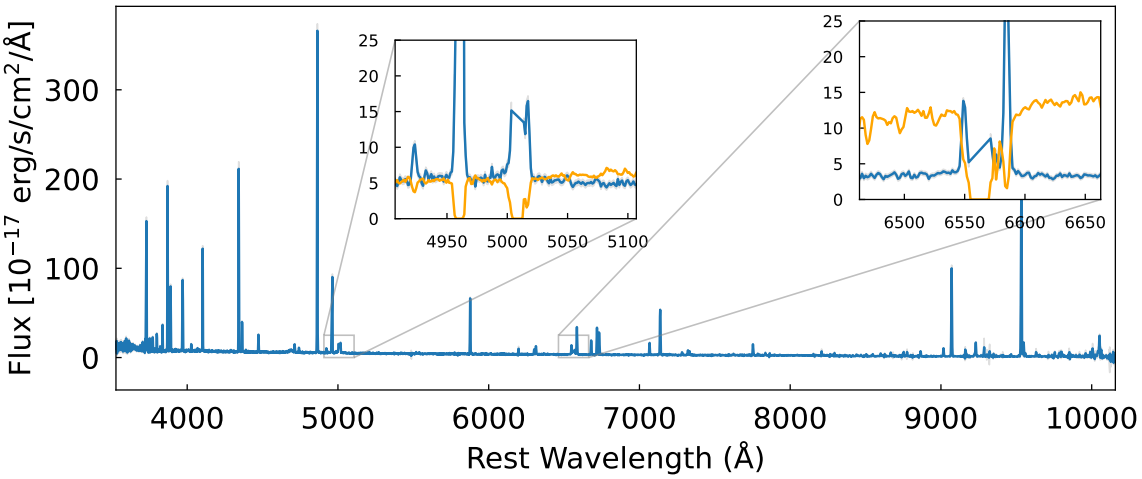


Figure 9. The spectrum (Plate: 11294; MJD: 58451; Fiber: 0164) for a galaxy with clipped emission lines. The spectrum is shown in blue, the error in light gray, and the inverse variance in orange. Two zoomed-in windows at [OIII] λ5008 (left) and Hα (right) have been added to demonstrate that the flux for these two lines has been masked out, as shown in orange, where the clipped lines coincide with an inverse variance of 0, which is a marker of bad data in SDSS. This effect is present in some galaxies with high EW emission lines and low gas velocity dispersions. See §2.5.

We chose to base our code on the MaNGA-DAP for several reasons. The eBOSS and MaNGA datasets use the same spectrograph and have similar, but not identical, data structures (plates vs. cubes), allowing many methods to be used with minimal modification. We also chose the MaNGA-DAP for its modular capabilities. We were able to fully customize our template libraries, line lists, and spectral indices, as well as the data that is saved. Another boon is the ability of the MaNGA-DAP pipeline to run on many spectra simultaneously, significantly reducing computational time for our 1.9 million spectra. Another key feature is MaNGA-DAP's ability to tie various emission line properties (line widths, velocity offsets, flux ratios) across multiple lines (F. Belfiore et al. 2019), using the implementation provided by pPXF. This allows us to use stronger lines to ensure robust fits for weaker lines by limiting some of their free parameters.

3.2. *The eBOSS-DAP*

To adapt the MaNGA-DAP for the goals of the eBOSS-DAP, we made several key changes to the code and supporting files, which fall into two classes: infrastructure changes and scientifically motivated changes.

Our first major infrastructure change was to enable the code to accept folders of one-dimensional spectra obtained on the same plate instead of single spectra or cubes. The details surrounding this change are found in §3.3. Additionally, we changed the preprocessing for the foreground Milky Way dust extinction correction. We use the `dustmaps` package (G. Green 2018) to retrieve the Milky Way E(B-V) value at the position of each target from the Corrected Schlegel, Finkbeiner & Davis (1998) dust maps (CSFD; Y.-K. Chiang 2023). We remove the foreground reddening from each spectrum using the `dust_extinction` code (K. D. Gordon 2024) with the K. D. Gordon et al. (2009) Milky Way dust attenuation law instead of the J. E. O'Donnell (1994) curve used for MaNGA.

An additional change was modifying the masking routine for the data, as eBOSS has slightly different mask bits than MaNGA. Our final set of infrastructure changes was fixing some minor issues we uncovered through our testing. For example, we found that if an emission line had only a few unmasked pixels, poor Gaussian fits could result. We, therefore, only report the results of the Gaussian fit for emission lines with less than 50% of their pixels masked out. We discuss the masking procedure further in §3.2.1. In addition, we only report spectral indices with less than 10% of their pixels masked out, as spectral indices are more sensitive to masking.

The first scientifically motivated change was to modify the spectral template libraries that the code relies upon. The MaNGA-DAP is configured to be able to use several different stellar population template libraries (see discussion in Abdurro'uf et al. 2022). These templates can be composed of individual stellar spectra or simple stellar population (SSP) models. We added a new SSP library called C3K that is discussed in detail in §3.2.2. We also made changes to the list of emission lines and line indices as detailed in §3.2.3 and §3.2.4.

3.2.1. *Masking*

The eBOSS data reduction pipeline creates a mask array that encodes data quality information differently from MaNGA.[6] Accordingly, we had to implement our own masking routine. When fitting the data, we chose to use a combination of masks, primarily the AND_MASK[7] and our own mask based on the inverse variance. The AND_MASK is a bitmask that flags pixels that were masked in every exposure contributing to the final spec-

[6] for further reference, see https://www.sdss4.org/dr17/algorithms/bitmasks/

[7] The particulars of the AND_MASK are found here: https://www.sdss4.org/dr17/algorithms/bitmasks/#SPPIXMASK

trum; the bits encode the reason for masking. This mask was then trimmed down by removing certain bits that we found via visual inspection to be masking apparently good data, namely, bit 23: BRIGHTSKY, as well as bits 0-12, which are so-called FIBERMASK_BITS[8] that mask the full spectrum. These bits are flagged when an error that would affect the full spectrum occurs, such as when the flat field is flagged as bad. There are 27,620 spectra or $\sim$ 1.5% of our sample where a FIBERMASK_BIT is set. We chose to fit these spectra, but we add a boolean column, FIBERMASKED, to the final output catalog indicating whether any FIBERMASK_BIT was set for that spectrum, rather than reporting the underlying hexadecimal mask value. After masking the pixels identified in our trimmed mask, we added any pixels for which the inverse variance array was negative, infinite, or zero.

In addition to masking pixels on *input* to the eBOSS-DAP, the analysis of the data leads to additional masking. The two primary masks indicate where the model is invalid (e.g., where the rest wavelengths of the template and galaxy spectra do not overlap) and which pixels in the galaxy spectra were rejected as outliers during the full-spectral fitting.

Our final additional mask consists of pixels in the window 3662 – 3706.3 Å and it is set only for stellar continuum and emission line fitting. This mask is created to avoid contamination of the continuum fit by high-order Balmer emission lines, which, as they are unfit by our code, pull up the continuum fit artificially. This mask is removed during spectral index measurement. The final mask is saved in the final output file for all spectra.

3.2.2. *C3K Spectral Libraries*

For our template library, we chose to generate SSPs and continuous star formation models based on the C3K stellar library (Conroy et al., in prep.) and MIST isochrones (A. Dotter 2016; J. Choi et al. 2016) found in the Flexible Stellar Population Synthesis (FSPS) package (C. Conroy et al. 2009; C. Conroy & J. E. Gunn 2010). The C3K model library, described in C. M. Byrne & E. R. Stanway (2023), consists of fully theoretical stellar spectra created using the ATLAS12 (F. Castelli 2005; R. L. Kurucz 1970) and SYNTHE (R. L. Kurucz 1993) codes. These models have stellar effective temperatures of 2500 $\leq$ T_{eff} $\leq$ 50,000, surface gravities of -1 $\leq$ $\log g$ $\leq$ 5.5 and metallicities 0.003 $\leq \frac{Z}{Z_\odot} \leq$ 3.16.

Approximately 80% of the eBOSS galaxy sample is at $z = 0.4 - 1.1$, which means that the blue edge of the spectrum is at restframe 1700 – 2600 Å. We chose to use the C3K SSPs primarily because most empirical models have limited UV coverage and/or low UV spectral resolution. Theoretical models also provide a denser exploration of parameter space (T_{eff}, $\log g$, Z), which can be important in achieving an optimal fit (P. R. T. Coelho et al. 2020). Additionally, the C3K models have higher spectral resolution than our data over most of the relevant wavelength range. Unlike observational data, they are unaffected by factors like flux calibration errors or sky subtraction residuals. Additionally, theoretical SSP models have been shown to better recover the ages and metallicities of star clusters (R. Asa'd et al. 2025). However, their precision is limited by the precision of the underlying atomic and molecular data, as well as the computational models used to generate them. (C. Conroy 2013; P. R. T. Coelho et al. 2020).

For our SSP model grid, we chose four metallicity bins and 18 age bins as seen in Figure 10. These ages were selected such that periods of rapid evolution received more finely binned SSPs to provide good coverage of different spectral shapes. Our youngest SSP model is 12.1 Myr old. To fit galaxies with ongoing star formation, we add two models that represent 5 and 10 Myr of continuous star formation. We adopted this approach to minimize the number of models needed. Because we are fitting galaxy spectra, they are unlikely to have changes in their star formation histories on timescales shorter than 5 Myr.

We use FSPS to add nebular continuum to our continuous star formation models. (We did not add it to our SSPs because nebular continuum does not contribute significantly to stellar populations older than 10 Myr (N. Byler et al. 2017).) We found that for galaxies with high levels of ongoing star formation, nebular continuum is needed to properly fit the spectrum at 3600-3700 Å as seen in Figure 11, panel **A**. If nebular continuum flux is not present in the models, the continuum will be underestimated blue-ward of the Balmer jump ($\sim$ 3645 Å) while being overestimated red-ward. Additionally, this can cause a loss of measured flux in [O II]$\lambda\lambda$ 3727, 3729, a critical emission line, illustrating how differences in the continuum treatment can propagate into emission-line measurements A second concern is that, although the eBOSS-DAP does not measure Balmer lines bluer than H12, there is significant continuum infilling from closely packed high-order Balmer lines (H14→H30) as shown in Figure 11 panel **B**. If the nebular continuum is not included in the fit, all of this flux is inappropriately attributed to the stellar continuum. If the high-order Balmer line fluxes are added by scaling the lines to H12, the models with nebular continuum included provide a superior fit in the 3500-3800 Å region.

The wavelengths of the C3K models natively span from 100 – 10^7 Å; however, for our models used in emission line fitting, we trimmed to 1281 – 10616 Å. The resolution of the C3K SSPs created by FSPS is $R \sim 1180$ between 1281 – 2750 Å, $R \sim 7060$ between 2750 – 9100 Å, and $R \sim 1180$ between 9100 - 10616 Å. For models used to fit the stellar continuum kinematics, we further restrict them to the $\lambda = 3000$ Å – 9000 Å range, with $R \sim 7060$. The spectral sampling of the C3K templates is also not uniform, meaning that we need to resample the spectra before the eBOSS-DAP can use them. To match the average sampling step across the wavelength range of our

[8] Definitions of the individual FIBERMASK_BITS (bits 0–12) are given here: https://www.sdss4.org/dr17/algorithms/bitmasks/#SPPIXMASK

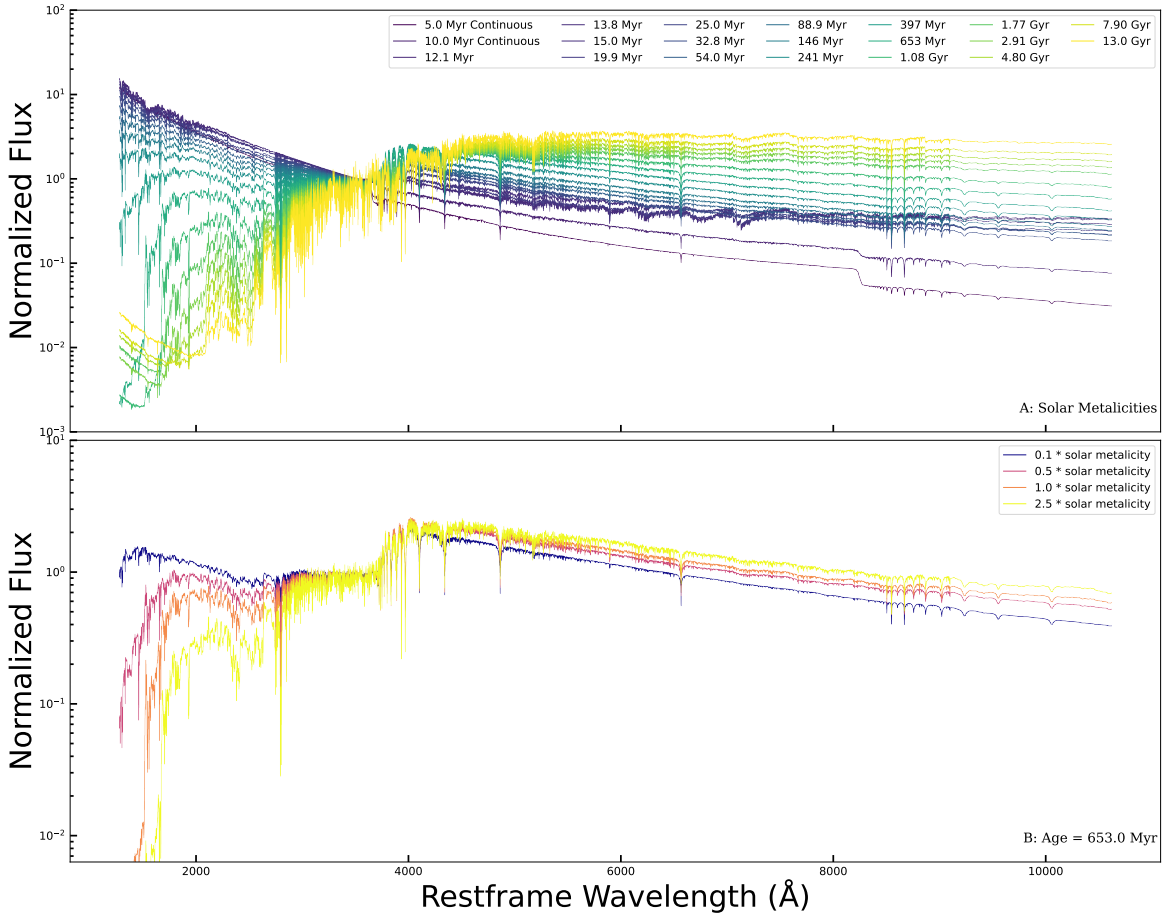


Figure 10. Stellar population templates employed by the eBOSS-DAP. The templates have been generated with FSPS (C. Conroy et al. 2009; C. Conroy & J. E. Gunn 2010) using the C3K stellar library (Conroy et al., in prep.). **Top:** Solar metallicity SSPs and two continuous models color-coded by age. **Bottom:** Four SSPs that share the same age of 653 Myr but vary in metallicity from $Z = 0.1 - 2.5\ Z_{\odot}$. The full template library includes all ages shown at all four metallicities (80 templates, in total). All templates are normalized to their flux at 3500 Å.

models, we resample the templates such that they are uniformly sampled in log space with a spectral spacing of $\mathrm{d}\log\lambda = 7.239 \times 10^{-5}$ or 49.97 km s^{-1}. The templates are then resampled again by the DAP to match the wavelength array of each plate.

3.2.3. *Emission Line Fitting*

The MaNGA-DAP natively provides users with a flexible and modular file that details the emission line list. What sets this fitting routine apart is the ability to tie parameters of the lines, namely the flux, velocity, and velocity dispersion. Line tying (as described in K. B. Westfall et al. (2019) with features implemented in M. Cappellari (2012, 2023)) refers to requiring the parameters of two or more separate lines to be related to each other, for example: [OIII] λ4960 flux = 0.331 [OIII] λ5008 flux. More specifically, when tying the flux of two lines, one free parameter effectively governs the flux of both lines in the model, and the fitting algorithm adjusts that parameter to optimize the fit to both lines simultaneously. Table B1 stores the emission line information, including the ratios and the lines used for tying.

A new feature in the eBOSS-DAP (which was possible but unused in previous MaNGA-DAP analysis) is the ability to specify that two line parameters be within some fractional range of each other. This can be seen with the example of [O III] λ5008 in Table B1. Here, the line list specifies that the [O III] λ5008 line must have equal velocity to Hα (in the low redshift bin), but the velocity dispersion is free to be within 75% of the Hα dispersion (i.e., $1/1.75\ \sigma_{\mathrm{H}\alpha} < \sigma_{[\mathrm{O\ III}]} < 1.75\ \sigma_{\mathrm{H}\alpha}$). We chose to impose this velocity dispersion tie on all lines, as it helps weak lines to be fit accurately and does not have adverse consequences for the stronger lines.

The allowed range in dispersion ratios ($\sigma_{\mathrm{line}} = 0.57$ - $1.75\ \sigma_{\mathrm{H}\alpha}$) was selected after empirically testing the range of dispersion ratios found for strong emission lines when no velocity dispersion tie was used. It accommodates the wavelength-dependent instrumental resolution and allows for real physical differences between emission lines produced in different regions of a galaxy, for example, [O III] lines in the narrow line region of Type II AGN. Note that Type I AGN, which can have extreme velocity dispersion differences between Balmer and forbidden lines, are generally not included in our sample, as they are classified as quasars rather than galaxies by the SDSS `spectro1d` pipeline which measures redshifts and spectral classifications.

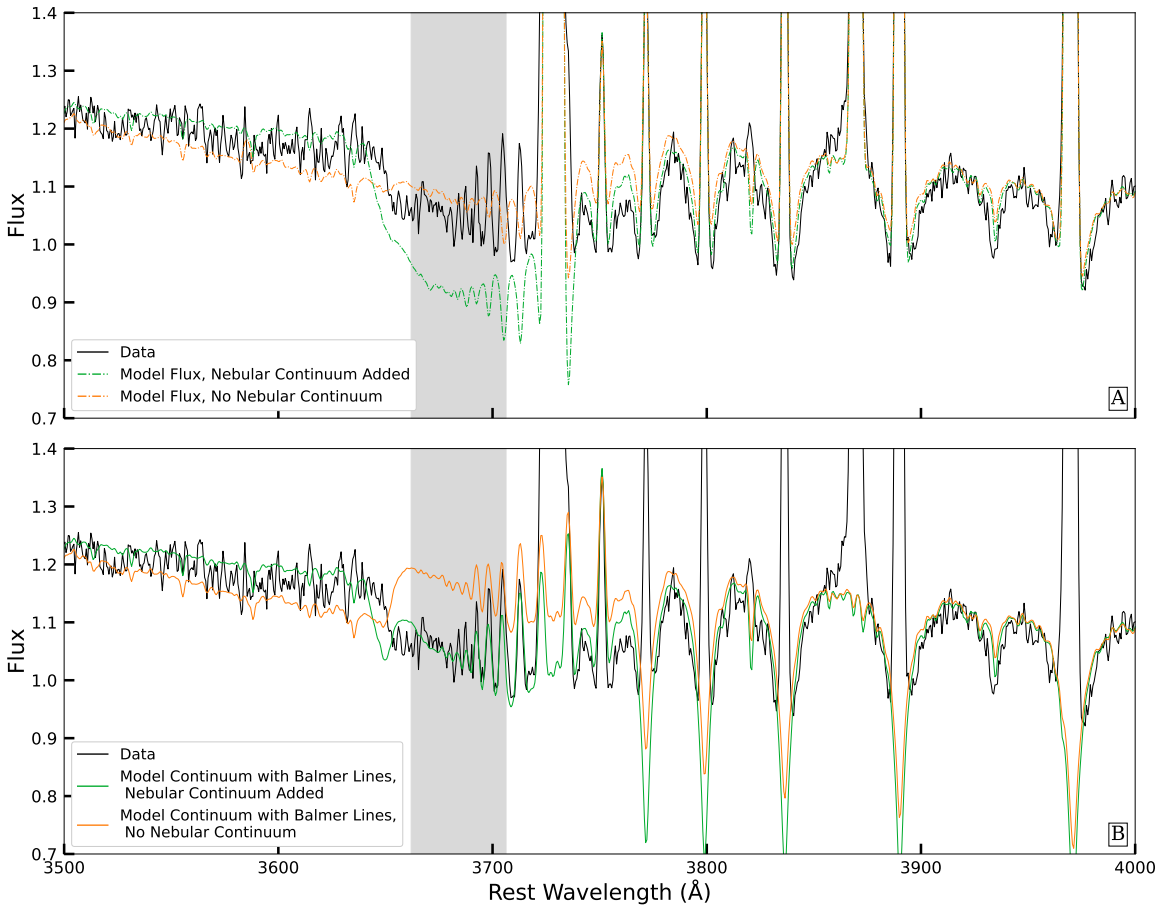


Figure 11. A comparison of stellar population models with and without nebular continuum. In both panels, the black line shows a stacked spectrum made from galaxies with very high Hβ EW, the orange line is the best-fit stellar population model when templates that do not include nebular continuum emission are used, and the green line is the best-fit model with nebular continuum included. The vertical gray band indicates the mask that is applied during fitting because the eBOSS-DAP does not model Balmer lines above H12 (see 3.2.1). **Panel A**: The full best-fit model fluxes for this stack, including all fitted emission lines. The models without nebular continuum (orange) underestimate the continuum blueward of 3662 Å and overestimate it redward of 3706 Å. The models with nebular continuum correctly estimate the continuum outside of the masked region. **Panel B**: The stellar continuum from the same best-fit models, with flux from high-order Balmer lines added to the continuum fits by scaling to the measured H12 flux assuming Case B line ratios. When the high-order Balmer flux is included, the models with nebular continuum provide a superior fit across the full wavelength range shown.

The eBOSS-DAP makes several additions to the MaNGA-DAP emission line list provided by DR17 (K. B. Westfall et al. 2019; D. R. Law et al. 2021a). The list is increased to 80 lines, of which only 35 were fit in MaNGA. The 43 new eBOSS-DAP lines are demarcated by an asterisk in Column 1 of Table B1. These lines include all iron lines found in the line list and all lines of $\lambda < 3600$ Å. Of particular note are [Ne V] $\lambda\lambda$3347, 3427 and [Fe X] λ6374, which are used as AGN diagnostics. The bluest line we fit is [C III] $\lambda\lambda$1906,1909, which redshifts into the observed spectral range at $z = 0.87$.

Unlike the MaNGA-DAP, which uses one line list for the entire sample, we use four distinct line lists that split our sample by Hβ equivalent width (EW) and by redshift. This was done in an effort to resolve two major problems: data size and restframe wavelength coverage.

Initially, we were fitting all lines in all spectra, but we noticed that our weaker lines returned measurements consistent with noise in the majority of spectra. Therefore, we elected to split the sample into two subsamples: one with an Hβ EW > 10 Å resulting in 167,466 spectra, and another with Hβ EW < 10 Å resulting in 1,734,368 spectra. All lines were fit in the high EW subsample, but in the low EW sample, a 27-line subset, made up of typically stronger lines, is fit. These lines are flagged in the last column of Table B1.

Our second division is a result of the wide redshift range of our data. A practical limitation of the MaNGA-DAP is that it must designate a reference line when setting up the set of tied emission lines. The line chosen is effectively irrelevant to the optimization algorithm, but the tying setup fails if the reference line is outside of the observed spectral range. This means that, while we may like to tie all of our lines to Hα, if it is outside of our observable window, all lines tied to it are not fit, regardless of whether the tied lines are observable. To remedy this, we made a redshift cut, and for all spectra above $z = 0.4963$, we tied lines to Hβ instead. We chose this redshift cut as this is when Hα enters a zone of increased measurement error near the edge of the spectrum, as seen in Figure 6. Roughly 60% of our sample lies above this redshift threshold, drastically increasing the quantity of

data we can successfully process.

To evaluate the impact of these divisions on the consistency of our emission–line measurements, we selected a random subsample of 4171 spectra satisfying $9 < \mathrm{EW}_{\mathrm{H}\beta} < 11$ Å and $0.1 < z < 0.4$, ensuring that all objects lie near the equivalent–width boundary while retaining all relevant lines within a regime of low spectrophotometric error. We find no systematic offset introduced by either the EW-based line-set division or the redshift-based anchor-line change; in both cases, the mean percent difference between configurations is consistent with zero for all six lines considered, and the mean difference normalized by the propagated measurement error reaches at most ∼8% of the measurement uncertainty. Any differences between configurations are consistent with random measurement noise. Full details of these comparisons, including per-line statistics, are provided in Appendix E (Figures E1 and E2; Tables E1 and E2). For access to the underlying per-object flux measurements for the two comparisons discussed above, see Data Availability.

3.2.4. *Spectral Indices*

Following K. B. Westfall et al. (2019), we adopt the term "Spectral Index" to refer to measurements of stellar continuum features. We have not changed any details of the spectral index measurements or outputs as specified in Table 4 of K. B. Westfall et al. (2019) and Section 5.2.2 of Abdurro'uf et al. (2022). Our singular contribution is the addition of a "BalmerBreak" index. We adopt the definition of B. Wang et al. (2024), which is measured identically to D4000 but with a blue bandpass of λ = 3620.0 – 3720.0 Å and a red bandpass of λ = 4000.0 – 4100.0 Å in vacuum wavelengths. This additional index allows us to measure the Balmer break, which appears as a discontinuity or "jump" in the stellar continuum spectrum at around 3645 Å. This break is caused by the ionization of hydrogen atoms from the second energy level within stellar atmospheres, leading to a drop in intensity at wavelengths shorter than this limit. The Balmer break is prominent in SSPs with ages of 0.3 - 1 Gyr, and it is therefore used in estimating the age of stellar populations and inferring the star formation history of galaxies.

3.3. *Workflow*

Running the eBOSS-DAP first requires a few setup steps. For each galaxy, we collect the foreground Milky Way E(B-V) value from the CSFD (Y.-K. Chiang 2023) maps in the `dustmaps` (G. Green 2018) package and the galaxy redshift from the `spAll-v5_13_2` file released in DR17. The sample is then divided into "low-z" and "high-z" samples, distinguished by those galaxies below and above $z = 0.4963$, respectively. Galaxies in the low-z bin tie all emission lines to Hα, whereas the high-z samples use Hβ; recall, this is largely a practical matter dictated by the use of the DAP. We also divide the sample into "low-EW" and "high-EW" samples based on a preliminary measurement (using the DAP) of the Hβ EW being below or above 10 Å, respectively. All emission lines are fit for galaxy spectra in the high-EW sample, whereas only a subset of the strongest lines are fit to the low-EW sample; see Table B1. The division by z and EW leads to four samples of spectra to be fit.

Spectra in each sample are fit in groups based on their plate number. This grouping is also primarily a practical issue: Each spectrum is treated independently, but this grouping allows us to perform common preparation steps (like building the spectral template library) once for a large number of spectra, instead of once per spectrum. The detailed steps performed for each spectral group (which closely follow the steps for the MaNGA DAP described by K. B. Westfall et al. 2019) are as follows:

(1) The spectral templates are resampled to the pixel scale of the galaxy data divided by an integer, N. Here we choose N=4 such that the line-spread function of the C3K templates (see §3.2.2) is still well-sampled. Due to C3K's varying spectral resolution, two spectral libraries are created. The first has coverage of λ = 1280 Å – 10600 Å ($R \sim 1180 - 7060$) and is used to measure the stellar continuum and emission lines. The second has coverage of λ = 3000 Å – 9000 Å ($R \sim 7060$) and is used to measure the stellar kinematics.

(2) The galaxy spectra are packaged into two-dimensional arrays with a common wavelength vector by adding modest zero-padding. The padded spectral regions are included in the masks (see Section 3.2.1). The observed fluxes and uncertainties are corrected for Milky Way extinction using the E(B-V) values and the `dust_extinction` (K. D. Gordon 2024) package using the K. D. Gordon et al. (2009) Milky Way extinction law. Masks from §3.2.1 are applied.

(3) The stellar kinematics are measured for each spectrum independently using pPXF (M. Cappellari 2023). The emission lines are masked during this fit, and we use an eighth-order polynomial in (additive) combination with the spectral templates with the shorter spectral range to model the continuum. See K. B. Westfall et al. (2019), Section 7.[9]

(4) The emission-line properties (flux, velocity, and velocity dispersion) are modeled simultaneously with the continuum templates, where the stellar kinematics are fixed to the results from the previous step. The continuum templates used include nebular continuum emission in the two continuous models as discussed in §3.2.2. For this module, the continuum templates used are those with the longer wavelength range, and we include an eighth-order *multiplicative* polynomial to apply low-order continuum modifications to address attenuation. Additionally, this polynomial helps minimize issues related to

[9] Measurements of the stellar velocity dispersion that exceed 450 km s^{-1} are considered erroneous. The output database replaces such measurements by imposing this upper limit, setting $\sigma_* = 450\,\mathrm{km\ s^{-1}}$.

flux-calibration errors and differences between the template library and the data. The best-fitting model Gaussian profiles for each emission line are then used to calculate their equivalent widths. The continuum for the EW measurements is defined by a line connecting the median flux in two passbands (red and blue, as defined in the input file) to the (unweighted) center of each passband. The continuum level used in the EW calculation is the value of this line at the fitted center of the emission line.

(5) In addition to the emission-line properties measured from the best-fitting Gaussian function, we also measure emission-line fluxes and EWs by direct integration of the continuum-subtracted spectrum. The code utilizes two sidebands to normalize any deviations from the continuum by drawing a line that passes through the coordinates defined by the center of each passband and the median flux within the passband. The continuum value is taken as the value of that line at the (measured) emission-line center. See K. B. Westfall et al. (2019), Section 9, and F. Belfiore et al. (2019) for further details. We only report the EW measurements, which are primarily used as a fit-quality metric; i.e., the EWs measured using the best-fit Gaussian and direct integration should be statistically identical for high-quality fits (see §4.2.1).

(6) The last analysis step is to measure the set of spectral indices described in §3.2.4 for our eBOSS spectra, after first subtracting the best-fit emission-line-only model. See K. B. Westfall et al. (2019), Section 10, and Abdurro'uf et al. (2022), Section 5.2.2.

(7) Finally, the analysis results are saved to a FITS file, one file per spectrum. Additionally, all non-detections and failures have both the signal and error overwritten with -999.0, the eBOSS-DAP error code. Once the analysis of all spectra is complete, the individual output files are aggregated into our final output catalogs; see Section 4.1.

4. RESULTS

We ran the eBOSS-DAP on a sample of 1,901,834 galaxy spectra with 1,899,553 successfully passing the full pipeline, giving us a 99.88% success rate. Figure 12 shows an example of the eBOSS-DAP's continuum and emission line fits. Two additional spectra are shown in the Appendix (Fig. D1, Fig. D2). [10] Panels A – E showcase the quality of our continuum fits, zooming in on some important spectral features. Similarly, panels F – L zoom in on several important emission lines and show that our line fitting is robust.

In §4.1 we discuss the catalogs generated by the eBOSS-DAP. In §4.2, we assess the quality of the catalog data by comparing measurements made on duplicate spectra and comparing to some existing catalogs in the literature. Finally, in §4.3, we present a series of plots that further characterize the eBOSS sample and illustrate its scientific potential.

[10] These plots are not generated as part of the eBOSS-DAP; they are generated by a separate program found here: https://github.com/owenmatthewsa/ebossdap/

4.1. *Catalogs*

We use the eBOSS-DAP outputs to create two emission line catalogs: one for the full sample (`eBOSS_DAP_emlines_full_v#.fit`; 1,899,553 spectra, which utilizes the reduced emission line list (27 lines), and one for the high equivalent width (Hβ EW $>$ 10 Å) sample (`eBOSS_DAP_emlines_high_ew_v#.fit`; 167,466 spectra), which makes use of the full line list (80 lines). The column descriptions of these catalogs are found in Table C1. All emission lines are corrected for foreground Milky Way reddening as described in Step **(2)** in §3.3. Notably, we include, along with the emission line velocity dispersions, the instrumental dispersion corrections made to the dispersions. In cases where the instrumental resolution exceeds the measured line width, the dispersion has been flagged as a poor fit.

The final two catalogs are the spectral indices and the stellar population template weights, along with auxiliary data. The `eBOSS_DAP_spind` table contains the spectral index catalog and the column descriptions given in Table C2. To find the units of a particular spectral index, readers should refer to the table of spectral indices (Table 4) in K. B. Westfall et al. (2019). These spectral indices are not corrected to a fixed velocity dispersion, as they were in the MaNGA-DAP; however, the corrections are included in the catalog if needed. The `eBOSS_DAP_auxdata` table contains the template grid weights as well as the multiplicative polynomial values and other auxiliary data required to produce the model as described in Table C3.

To help visualize the eBOSS-DAP catalog, we have produced the following two figures. In Figure 13 we show a set of S/N histograms for our Gaussian fits to 12 commonly used emission lines in our catalog, annotated with the number of detections of S/N$>$ 5 in each line. Of note is the large quantity of galaxies with [Ne V] S/N $>$ 5. We will explore these objects further in future work (Matthews Acuña et al., in prep.).

In Figure 14 we show a histogram of the errors in four popular spectral indices. Due to the way spectral indices are measured, values may be positive or negative. S/N measurements are misleading when the index values approach zero, so we elected to simply show the errors in these indices. We additionally include the number of spectra in D_n4000 and Hδ_A which pass the quality cuts suggested in G. Kauffmann et al. (2003) of D_n4000 error < 0.03 and Hδ_A error < 0.8.

4.2. *Data Quality Assessment*

We will assess data quality in three ways: Comparing Gaussian and direct integrated EWs (§4.2.1), comparing eBOSS-DAP data with SDSS pipeline emission line measurements (§4.2.2), and comparing measurements made on repeat spectra (§4.2.3).

4.2.1. *Gaussian vs Integrated EW Comparisons*

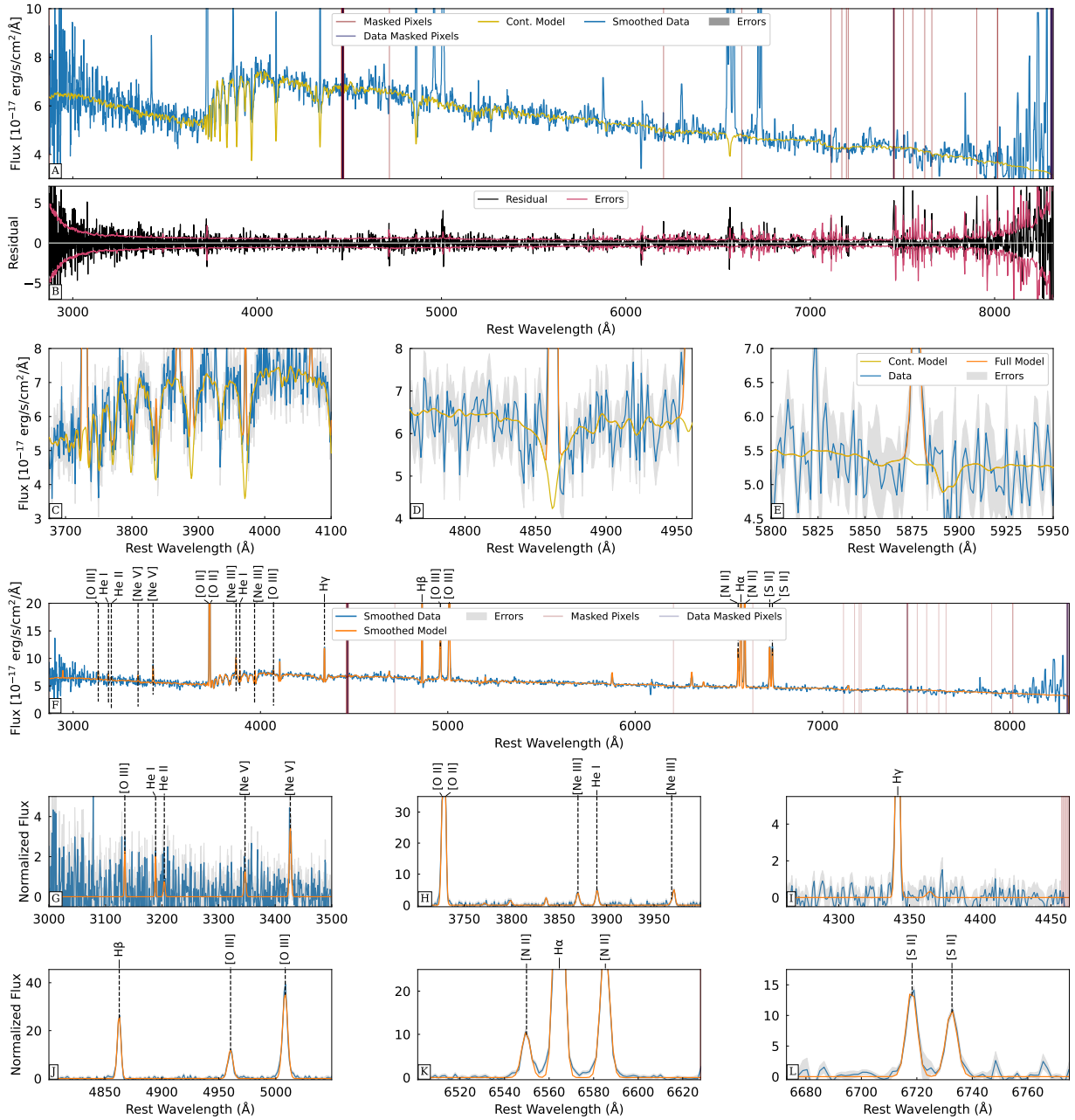


Figure 12. Sample eBOSS-DAP fit for the spectrum spec-4037-55631-0920.fits, which was categorized as an AGN using the Baldwin, Phillips, and Terlevich (BPT) (J. A. Baldwin et al. 1981) diagnostic. In all panels, the processed data are shown in blue. The best-fit continuum model is shown in dark yellow. The full best-fit model, including emission lines, is shown in orange. The masked portions are shown as vertical red bars. Errors are shown in gray bands. **Panel A:** A zoomed-in view on the smoothed continuum to demonstrate the quality of the fit. **Panel B:** The residual of the full model fit (black). There is a white line at zero for legibility and a red line showing the errors on the residual. **Panels C, D, and E:** Zoomed-in windows showing the continuum fit near some strong stellar absorption lines: the low-order Balmer lines (C), Hβ (D), and Na I (E). **Panel F:** The full fit (stellar continuum plus emission lines) compared to the data. Emission lines are labeled. **Panels G-L:** Various zoomed-in locations of important emission lines, which have been labeled. These panels are continuum-subtracted, so the continuum flux is zero at all points.

We test the integrity of our Gaussian emission line fits by comparing the emission line equivalent widths (EWs) computed from the Gaussian fits to those found by integrating the continuum-subtracted spectrum between the line boundaries specified in Table C1. These integrated EWs should be within a standard deviation of the Gaussian EWs found by the model fitting and, as such, offer a check on the quality of any particular fit. Following F. Belfiore et al. (2019), we compare the Gaussian and integrated EWs by computing their percent difference as a function of S/N.

In Figure 15 we see that as S/N increases, the integrated and Gaussian EWs grow closer, as expected. Of note is that both Hα and [S II] have, on average, lower integrated EWs. This is caused by the narrow integration boundaries used for these lines due to the presence

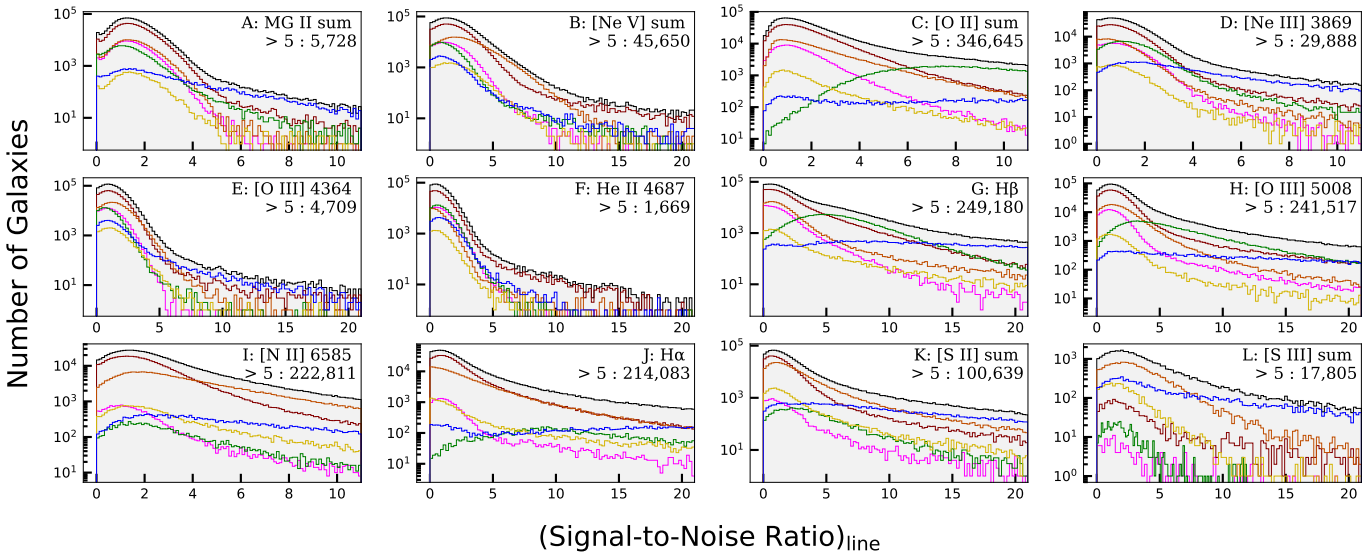


Figure 13. The S/N histograms of 12 lines in the eBOSS-DAP full sample, split by target classification. The target classes are color-coded identically to Fig. 1. Additionally, the number of galaxies that have S/N > 5 in the line flux has been included underneath the line name.

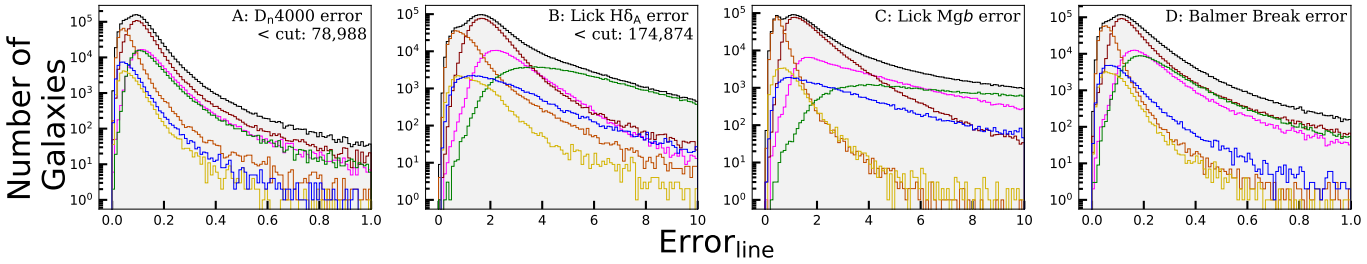


Figure 14. Histograms of the errors in four spectral indices in our full sample, split by target classification (see Fig 1 for color coding). Additionally, the number of galaxies that pass the quality cuts suggested by G. Kauffmann et al. (2003) are included underneath the index name for D_n4000 and $H\delta_A$ (see §4.3.5 for descriptions of these cuts).

of nearby lines (see Table C1). In most of the lines, the Gaussian and integrated EWs agree within the expected margin of error, with slightly higher deviations in Hα and [S II], likely caused by broader components outside of the integration bounds of those lines. Additionally, the [O III] and Hβ lines show higher-than-expected deviations, likely due to substructure that is not well fit by a Gaussian – for example, a low-level broad component. Both Gaussian and integrated EWs are included in the eBOSS-DAP catalogs.

4.2.2. *SDSS measurement Comparisons*

SDSS provides an emission line catalog for the eBOSS sample stored in the `spZline` files.[11] However, there are several issues with the SDSS `spZline` catalog that motivated the development of the eBOSS-DAP: the SDSS line list comprises only 27 lines compared to our 80; the emission lines are not corrected for Milky Way dust attenuation; and stellar absorption indices are not measured. Moreover, there is only minimal documentation available on the methods used to create the `spZline` catalog (A. S. Bolton et al. 2012). Nonetheless, it provides a valuable point of comparison for the eBOSS-DAP catalog.

[11] https://data.sdss.org/datamodel/files/BOSS_SPECTRO_REDUX/RUN2D/PLATE4/RUN1D/spZline.html

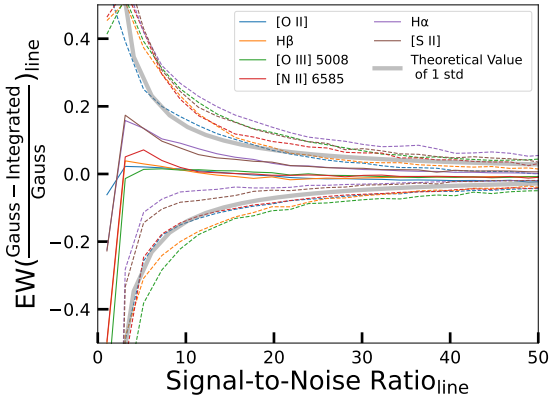


Figure 15. A comparison of Gaussian and integrated equivalent widths (EWs) relative to S/N for six commonly used strong emission lines. We take the Gaussian EW, subtract the integrated EW, and divide the result by the Gaussian EW to find the percent difference. Solid lines represent the median, while the dashed lines represent the standard deviation. A gray line has been included to show the expected value of the standard deviation given the S/N.

To compare the two sets of emission line measurements, we first corrected the `spZline` measurements for Milky Way dust attenuation using the same process as the eBOSS-DAP. We then plot the flux of an emission line found by the eBOSS-DAP divided by the flux in the

spZline catalog and compare it to the S/N of that line, as shown in Figure 16. Random variations are expected to produce a shape in which the standard deviation at any S/N is given by $\sigma \simeq \frac{\sqrt{2}}{S/N}$. In Figure 16, we compare the strong optical emission line fluxes of [O II] 3726,3729, Hβ, [O III] 5008, Hα and [N II] 6584, and [S II] 6718,6733. For most lines, the standard deviation of the flux measurements (pink points) decreases with S/N as predicted (orange lines), demonstrating the expected level of agreement between the eBOSS-DAP and the spZline catalog.

Hβ shows the most prominent difference in the two line flux measurements, being 0.128 dex higher on average in the eBOSS-DAP. This can be attributed to the fact that Hβ lies in a strong stellar absorption feature, which is modeled differently in the two codes. The SDSS code uses a Principal Component Analysis (PCA) approach and the ELODIE empirical stellar library (P. Prugniel & C. Soubiran 2001) to fit the stellar continuum (A. S. Bolton et al. 2012). The ELODIE library is known to be incomplete, especially for very hot stars and at non-solar metallicities (C. Maraston & G. Strömbäck 2011). In addition, PCA spectral reconstruction can sometimes produce non-physical spectra since the eigenvectors summed to create the final spectrum can be added or subtracted. Thus, it is likely that the eBOSS-DAP, with its non-negative combination of modern stellar population synthesis models (see §3.2.2), provides an improved stellar continuum fit and a more accurate Hβ flux.

Additionally, Hα shows a slight negative preference in the low S/N regime, while [N II] 6585 shows a slight positive preference. This is likely due to SDSS assigning flux from Hα to [N II] 6585 in low S/N data. [S II] 6718,6733 also has a slight positive preference, meaning that the eBOSS-DAP assigned it more flux in low S/N data than SDSS did.

4.2.3. *Repeat Spectra Comparisons*

Our final quality assessment was to make use of the 197,521 repeat spectra that eBOSS took to test consistency in measurements. In Figures 17 and 18 we plot the flux (or equivalent width) of an emission line divided by its value in a repeat observation and compare this ratio to the average S/N of the two observations. In Figure 17, we show the strong optical emission line fluxes of [O II] 3726,3729, Hβ, [O III] 5008, Hα and [N II] 6584. The standard deviation of the repeat data (pink points) decreases with S/N as predicted (orange lines), but shows some deviations at high S/N. This is due to variations in the spectrophotometric calibration between the repeat spectra (see §2.4.) Both statistical error and variations in spectrophotometric calibration drive differences in the fluxes measured in repeat spectra. In the low S/N regime, emission line differences are dominated by statistical error, which is well captured by the eBOSS-DAP (the pink 1-σ values of the data line up well with the orange theoretical lines). However, in the high S/N regime, the spectrophotometry errors become dominant, and then the difference between the repeat spectra becomes larger than our measured errors (the pink 1-σ values of the data lie outside the orange theoretical lines). Notably, equivalent widths are free from spectrophotometry errors. Consequently, the Hβ EW differences (Panel C) show improved agreement of the pink points and orange lines at high S/N, although the errors are still slightly underestimated.

In Figure 18, we show a comparison of the fluxes from repeat spectra of three intrinsically weak emission lines: [Ne V] 3426, [O III] 4364, and He II 4687. These lines are only detected at S/N$>$ 5 in $\sim$ 1% of the galaxies with repeat spectra, making our comparison statistics more marginal. Nonetheless, we observe some differences from Figure 17: for [Ne V] (and to a lesser extent [O III] 4364) at S/N$\simeq 2-6$ the pink points deviate from the orange lines, suggesting that the measured error of the line fluxes substantially underestimates the true error. Errors in the continuum fit can impact low EW lines such as these; however, the eBOSS-DAP fits the continuum simultaneously with the emission lines, and therefore, the associated error is included in the flux errors. Therefore, this is unlikely to be the source of the discrepancy. Notably, the strong emission lines in Fig. 17 show reasonable agreement between the predicted and actual errors at S/N $= 2-6$. For these weak lines, we suspect that rare spurious detections may outnumber real line detections in this S/N regime. The wavelength of [Ne V] 3426 also means that the line is commonly observed at the blue edge of the spectrograph, where the spectrophotometry errors are substantial (see §2.4). Users of the catalog are advised to exercise caution when conducting science with these and other weak lines and to utilize repeat spectra to better understand the appropriate detection threshold.

Unfortunately, it is not possible to accurately report the spectrophotometry error for an individual line flux measurement, as this depends on a complex interplay of plate drilling errors, telescope guiding errors, the airmass and seeing at the time of observation, errors in spectral typing the standard stars on the plate, etc. However, we used the repeat spectra to compute a scale factor that can be applied to the reported uncertainty of each line to approximately account for the additional uncertainty arising from spectrophotometric errors. These values are computed from the ratio of the measured errors to the 1-σ dispersion of the repeat spectra (e.g., the ratio of the pink points to the orange lines) for emission lines with S/N $>$ 3. Specifically, we fit $\sigma_{\rm measured} = \sqrt{(\sqrt{2}/(S/N))^2 + (\sqrt{2}\,a)^2}$, where a is the scale factor reported in Table 1. In Table 1, we list this recommended scale factor for some commonly used emission lines. We also report the scaling that should be applied to the errors of various common line ratios. These correction factors have lower values than for the line fluxes because they are only sensitive to changes in the shape of the spectrum rather than its zero-point. Readers are referred to §2.4 for additional details on the spectrophotometric calibration.

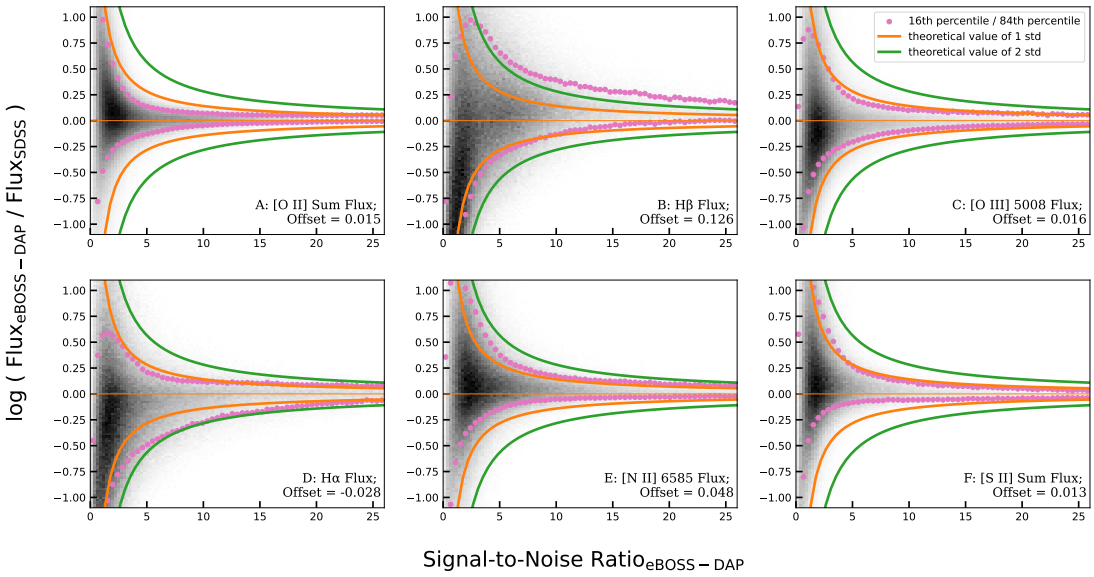


Figure 16. A comparison of line flux measurements in the eBOSS-DAP and the SDSS `spZline` catalog for six relatively strong emission lines. The y-axis shows the log of the ratio between the flux from the eBOSS-DAP and the dust-corrected SDSS-provided measurement for the same object for a particular line. The x-axis plots the S/N of that observation in the eBOSS-DAP. The 1-sigma spread of the data is plotted in pink points, which can be visually compared to the expected value at a specific S/N, shown in orange and green lines at the 1-sigma and 2-sigma levels, respectively. The average offset for lines with S/N > 3 has been given for each line in the lower right of each panel. For access to summary tables for this figure see Data Availability

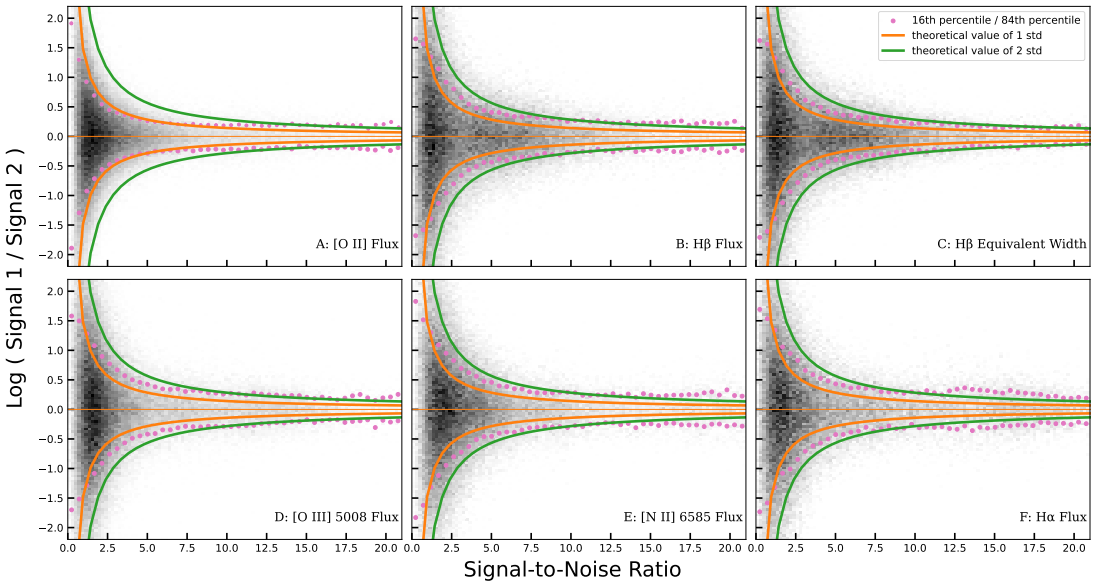


Figure 17. A comparison of line fluxes and EWs measured by the eBOSS-DAP in repeat galaxy spectra as a function of the emission line S/N. The data are shown in grayscale; pink dots show the 1-σ width of the distribution. Orange and green lines show the expected 1-σ and 2-σ spread of the data given the line S/N. Good agreement between the pink points and orange lines indicates that the errors on the emission line measurements are correct. **Panels A, B, D - F:** These panels compare fluxes of five relatively strong emission lines. At high S/N errors on the lines appear to be underestimated; this is a consequence of additional spectrophotometry errors; see §4.2.3. **Panel C:** This panel compares the variation in the Hβ equivalent width rather than flux. This variation is smaller than in the Hβ flux, as we expect EWs to be unaffected by spectrophotometric errors. For access to summary tables for this figure see Data Availability

Our final validation step was to assess the quality of our stellar continuum kinematics, in particular the stellar velocity dispersion σ_*, by comparing measurements made from repeat spectra. Figure 19 shows that the reported kinematic errors explain the variation in the pairs, requiring only a scaling of 1.29 on the error. Unlike the line-flux scale factors, this σ_* scaling is multiplicative: we fit $\sigma_{\rm measured} = \sqrt{2}/({\rm S/N}) \times a$, where $a = 1.29$. The stellar velocity dispersion is measured with an error of less than 50 km s^{-1} for 82.5% of the sample.

4.3. *Sample Characterization*

As part of this investigation, we have made a slate of figures of the data to provide a clear picture of the make-up of the eBOSS-DAP catalog and illustrate the catalog's possible uses: a mass–stellar velocity dispersion diagram,

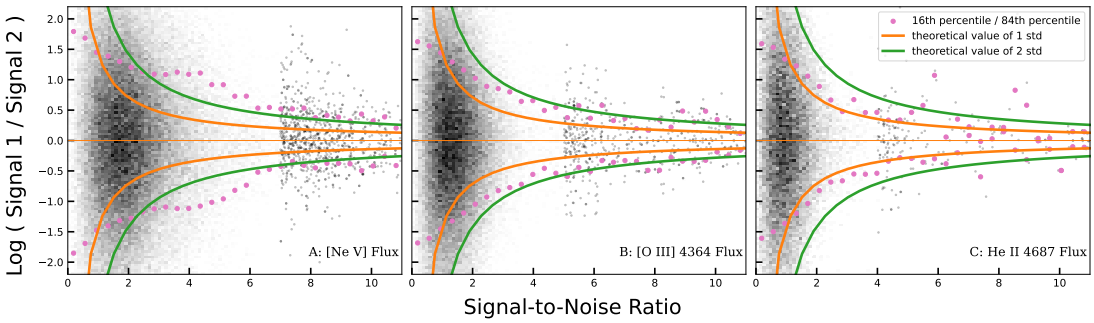


Figure 18. A comparison of line fluxes measured by the eBOSS-DAP for three weak emission lines: [Ne V] 3426, [O III] 4364, and He II 4687. These lines are only measured at S/N> 5 in ∼ 1% of galaxies. The data is shown in grayscale and plotted as individual points above S/N = 7, 5, 4 in panels A, B, and C, respectively. The colored lines are the same as in Figure 17. The discrepancy between the observed (pink points) and predicted (orange line) spread of the data at S/N = 2-6 in [Ne V] is likely due to spurious line detections at very blue wavelengths; see §4.2.3. For access to summary tables for this figure see Data Availability

Table 1: Uncertainty Scaling

Name	Recommended Uncertainty Scaling
[Ne V] 3427	0.114
[O II] 3727, 3729	0.097
[Ne III] 3869	0.129
[O III] 4364	0.138
He II 4687	0.188
Hβ	0.151
[O III] 4960	0.143
[O III] 5008	0.143
He I 5877	0.123
[O I] 6302	0.115
Hα	0.187
[N II] 6585	0.159
[S II] 6718	0.163
[S II] 6732	0.159
log (([O II] 3727 + 3729) / [O III] 5008)	0.077
log ([O III] 5008 / Hβ)	0.061
log ([N II] 6585 / Hα)	0.065
Hα / Hβ	0.08
σ_*	1.29

Note: For line fluxes, add the scale factor a times the flux in quadrature with the reported flux error, such that $\sigma_{\rm corrected} = \sqrt{\sigma^2_{\rm eBOSS-DAP} + (F_{\rm eBOSS-DAP} \times a)^2}$. The scaling on σ_* is multiplicative rather than additive: $\sigma_{*,\rm corrected} = \sigma_{*,\rm eBOSS-DAP} \times a$. See §4.2.3 for how these values were derived.

a BPT diagram, a star formation rate (SFR) vs stellar mass diagram, a mass–metallicity diagram, and a Hδ_A vs Dn4000 diagram.

The stellar masses are from a catalog of SED-derived parameters produced by D. Miller et al., in prep, using the Code for Investigating GALaxy Emission (CIGALE; M. Boquien et al. 2019). The inputs to the SED fitting are the SDSS redshift, the Legacy Survey *gri* photometry (A. Dey et al. 2019), the WISE (E. L. Wright et al. 2010) W1-W3 band photometry and the Dn4000 index measured by the eBOSS-DAP. The SEDs were computed by using a grid of parametric star-formation histories (a delayed τ model plus a burst), G. Bruzual & S. Charlot (2003) SSP models with a Chabrier IMF (G. Chabrier 2003), nebular emission, a D. Calzetti et al. (2000) dust attenuation law, and a B. T. Draine et al. (2014) dust

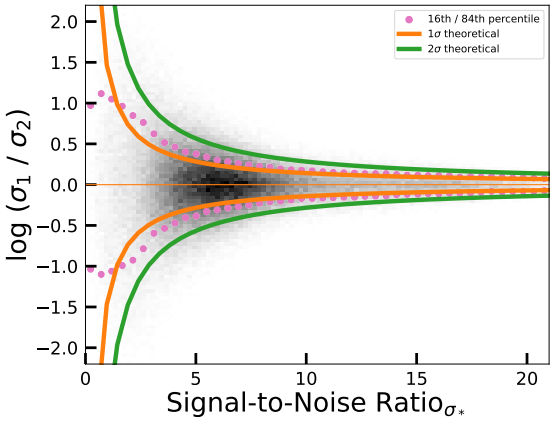


Figure 19. A comparison of the stellar velocity dispersions measured by the eBOSS-DAP in repeat spectra. The color coding is the same as in Figure 17. The reported velocity dispersion errors require a scaling correction of 1.29 to match the observed variation in the pink dots (see §4.2.3).

emission law. Typical errors on the stellar masses are ±0.07 dex.

4.3.1. *Mass–σ_**

In Figure 20 we show a plot of the stellar continuum velocity dispersion measured by the eBOSS-DAP versus stellar mass, M$_*$, measured from the photometry with CIGALE (D. Miller et al, in prep.). The eBOSS-DAP yields 1,449,940 stellar velocity dispersion measurements with error < 50 km s^{-1}, or 76% of the sample. Included in Figure 20 are best-fit lines to the $0.6 < z < 0.7$ Smithsonian Hectospec Lensing Survey (SHELS; M. J. Geller et al. 2005, 2014, 2016) sample and the $0.02 < z < 0.2$ SDSS main galaxy sample (M. A. Strauss et al. 2002) found by H. J. Zahid et al. (2016). The median relation for eBOSS is shown as a white line over the same mass range as these two samples ($9.0 < \mathrm{Log}(\frac{\mathrm{M}_*}{\mathrm{M}_\odot}) < 11.5$). Our data, which peaks at $z \simeq 0.55$, broadly agree with both the low-z SDSS sample and the higher-redshift SHELS sample. The eBOSS ELGs (shown in green) fall somewhat below the mean relation. These $z \sim 0.8$ star forming galaxies were selected based on their blue colors, which may have favored galaxies with small bulges and face-on orientations, leading to lower velocity dispersions. As an additional check, we compare the stel-

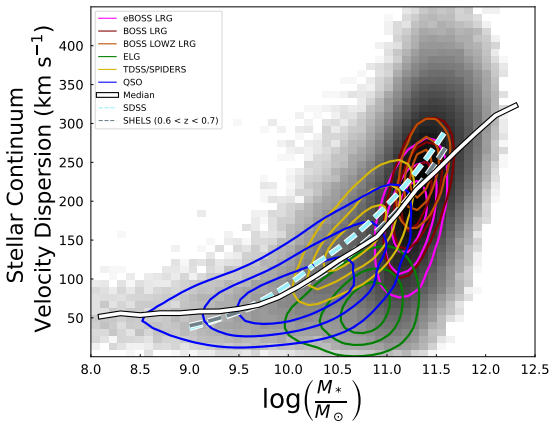


Figure 20. Stellar velocity dispersion vs. stellar mass for eBOSS galaxies with a stellar velocity dispersion error < 50 km s^{-1}. The grayscale is a 2D log-scaled histogram of the full sample. The contours show the different target classes; the outermost contour for each class encloses 75% of the total sample. The median relation is shown in white. The dashed lines show the median relation for the SDSS-I sample (light blue) and a high-z SHELS sample (gray) found in H. J. Zahid et al. (2016). The SDSS-I sample has a redshift range $0.02 < z < 0.2$, while the SHELS sample has a higher range ($0.6 < z < 0.7$). The eBOSS sample has a redshift range of $0.0005 < z < 1.12$ with a peak at $z = 0.55$.

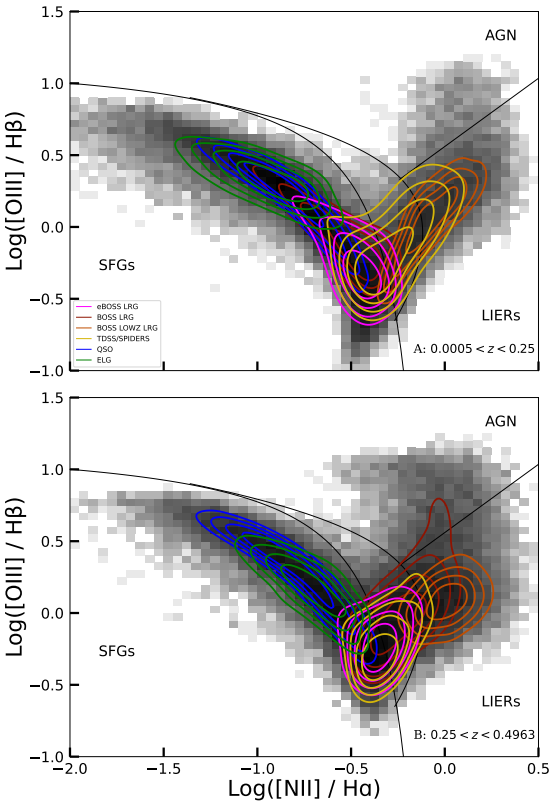


Figure 21. BPT diagram in two redshift ranges ($0.0005 < z < 0.25$ and $0.25 < z < 0.4963$). The eBOSS data are shown as 2D log-scaled histograms. Contours show the location of different target classes; they begin at 50% of the data. The diagram is divided into regions representing different ionization sources following D. R. Law et al. (2021b). 'AGN' are Active Galactic Nuclei, 'SFGs' are Star-Forming Galaxies, 'LIERs' are Low Ionization Emission Regions, and finally, the unlabeled region between SFGs and AGN is composite galaxies.

lar velocity dispersion to the Hβ emission-line width in Appendix F (Figure F1). The two measurements agree well in the mean across all target classes with the notable exception of the ELGs, which have stellar velocity dispersions $\sim$25 km s^{-1} smaller than their gas velocity dispersions, on average. The ELGs have the lowest continuum S/N of any of the target classes and it is unclear whether this difference is a systematic error or real physical effect. Notably, galaxies targeted as QSOs also have blue colors, but they tend to be compact and brighter than the ELGs; they do not show any discrepancies in either Figure 20 or Figure F1.

4.3.2. *BPT*

Our next example figure is the Baldwin, Phillips, and Terlevich (BPT) diagram (J. A. Baldwin et al. 1981) using the updated classification lines from D. R. Law et al. (2021b). The BPT uses a combination of $\log(\frac{\text{[O III] 5008}}{\text{H}\beta})$ (R3) and $\log(\frac{\text{[N II] 6584}}{\text{H}\alpha})$ (N2) to identify the origin of emission lines in galaxies. It is typically understood that N2 acts as a proxy for metallicity and R3 acts as a proxy for ionization level. Star-Forming Galaxies (SFGs) span a broad range of metallicity and ionization parameter, but the two are generally anti-correlated; e.g., high metallicity galaxies have low ionization parameter (X. Ji & R. Yan 2022).

AGN are typically found in massive metal-rich galaxies, and they can be a powerful source of hard ionizing photons, leading to high ionization parameters. Thus, the presence of an AGN will increase the R3 ratio as hard ionization from AGN will increase [OIII] (L. J. Kewley et al. 2013). Additionally, as AGN emission lines trace the Narrow Line Region (NLR) rather than interstellar medium (ISM) gas, [N II] emission will be much higher in AGN than in SFGs. This is because the NLR is far denser and hotter than the gas in the ISM, leading to much more collisional excitation, which [N II] is particularly sensitive to. As such, AGN will lie in the high metallicity (high N2) and high ionization (high R3) region, opposite from Star-Forming Galaxies (SFGs). Additionally, there are two other classifications: composite galaxies, which are a mix of AGN-like and SFG-like emission, and Low-Ionization Emission Line Regions (LIERs). LIERs are galaxies that see highly elevated N2 with low R3. It is unknown what mechanism drives emission in LIER galaxies; they exhibit AGN-like N2 levels, but this emission is sometimes detected far from the nuclear region, leading to debate about the cause of this radiation (F. Belfiore et al. 2016).

We first trimmed the sample down such that all BPT lines (Hβ, [O III] 5008, Hα, and [N II] 6584) were at S/N > 3, and then trimmed to a redshift range of $0.0005 < z < 0.4963$. We chose this redshift cut-off to prevent any possible systematic errors from switching the line tying from Hα to Hβ (see §3.2.3 for details). This resulted in 94,183 spectra or $\sim$ 12.4% of the sample in that redshift range. In Figure 21 we show the BPT diagram for this sample for redshifts below and above

$z = 0.25$. As shown in Fig. 21, the different target classes lie primarily in specific parts of the BPT diagram, with ELGs and compact blue galaxies mis-targeted as quasars (QSOs) lying primarily in the star-forming region, and the other target classes having some level of AGN contribution. Of note is that, in higher redshift bins, LRG classes are more likely to host AGN.

The BPT is usable up to $z = 0.5459$, at which point Hα is redshifted out of the observable window for eBOSS. Alternative AGN classification diagrams, such as MEx (S. Juneau et al. 2014) or OH-NO (L. J. Kewley et al. 2019), can be used at higher redshifts, although they suffer from reduced completeness and purity (N. J. Cleri et al. 2025).

4.3.3. *Star-Formation Rate vs Stellar Mass*

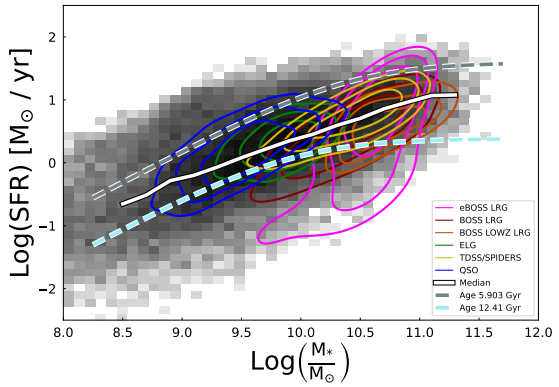


Figure 22. The Star-Formation Rate (SFR; found through Hα luminosity) vs stellar mass (M_*; found with CIGALE) diagram for star-forming galaxies at $0.0005 < z < 0.4963$. The eBOSS data for BPT-selected star-forming galaxies with S/N > 3 [O III] 5008 and [N II] 6584 lines and S/N > 5 Hβ and Hα lines is shown as a 2D log-scaled histogram (grayscale). Colored contours show the location of different target classes; contours begin at 50% of the data. The median line has been plotted in white; orange and blue lines show the star-forming main sequence from P. Popesso et al. (2023) at ages of 12.41 Gyr($z = 0.1$) and 5.903 Gyr($z = 1$), respectively.

Our third diagram is a Star-Formation Rate (SFR) versus stellar mass diagram, which is commonly used to identify star formation modes in galaxies: galaxies on the 'main sequence' are forming stars steadily, those above it are in a starburst phase, while those below may be quenching or already passive. Additionally, the star-forming main sequence evolves over redshift, moving towards higher average star-formation rates for galaxies at higher redshifts (c.f., P. Popesso et al. 2023). To make this diagram, we require [O III] 5008 and [N II] 6584 S/N > 3 and Hβ and Hα S/N > 5. The Balmer lines have a higher S/N cut as they are used to compute the extinction correction of the spectra before determining the star formation rate. We then trim the sample to include only galaxies that were classified as a BPT SFG using the D. R. Law et al. (2021b) lines. This resulted in 44,406 galaxies or $\sim 6\%$ of the sample in this redshift range ($0.0005 < z < 0.4963$), or $\sim 47\%$ of galaxies that pass the BPT cuts.

We compute the extinction corrected Hα luminosity by first computing E(B - V) from $\frac{H\alpha}{H\beta}$. We then use the same `dust_extinction` package to find the correction and apply it to the Hα flux. The Hα flux was then converted to luminosity and corrected for the fiber filling fraction (see §2.3 and Fig.4). We then calculate star formation rates for this subsample using the extinction corrected Hα luminosity and the R. C. Kennicutt & N. J. Evans (2012) calibration. We plot the 2D log-scaled histogram of the SFRs versus the masses of the subsample, as well as the star-forming main sequence from P. Popesso et al. (2023) for ages of 5.903 Gyr ($z = 1$) and 12.41 Gyr ($z = 0.1$) in Figure 22.

Our median lies comfortably between the two star-forming main sequences, chosen by finding the ages of the universe at the maximum and minimum redshifts of our sample. Additionally, we find that galaxies targeted as ELGs and QSOs have characteristically lower masses than the LRG targets, and they are more likely to be on the main sequence.

Of note is that we only show BPT SFGs in this figure. This is because we use Hα as our star formation rate indicator, and it is not a reliable indicator for BPT LIERs and AGN. These two populations typically fall below the main sequence (c.f., D. Miller et al., in prep.).

4.3.4. *Mass–Metallicity Relation*

Our penultimate sample characterization is the stellar mass – gas-phase metallicity relation (MZR). The MZR is extremely tight (± 0.1 dex) at $z \sim 0.1$ (C. A. Tremonti et al. 2004), and it has been shown to evolve mildly with redshift (H. J. Zahid et al. 2014; Z. J. Lewis et al. 2024). Galaxies classified as AGN according to the D. R. Law et al. (2021b) BPT diagram are removed from the sample, as are galaxies with [O II] 3727, 3729, Hβ, [O III] 5008, Hα, and [N II] 6584 lines with S/N < 3. These cuts yield 46,098 spectra, corresponding to roughly 73% of the 63,182 BPT SFGs. Metallicities are calculated according to the $\log(\frac{[\text{O II}]\ 3727,3729+[\text{O III}]\ 5008}{\text{H}\beta})$ (R23) diagnostic calibration of K. Nakajima et al. (2022), and the double-branching is broken using the excitation parameter $\log(\frac{[\text{O III}]\ 5008}{[\text{O II}]\ 3727,3729})$ (O32).

We plot our findings in Fig. 23. Panel A shows the MZR for our sample in the redshift range $0.0005 < z < 0.4963$ along with target classification contours. Here we see that LRGs have both higher masses and higher metallicities than ELGs and QSO targets. We grouped LRGs and TDSS/SPIDERS spectra (metal-rich, redder galaxies), as well as ELGs and QSOs (metal-poor, bluer galaxies), to find mass–metallicity relations for both broad classes of objects. These relations are observed to exhibit the expected correlation, including both the power-law rise at low stellar masses in ELGs and the metallicity saturation and plateau at higher stellar masses in LRGs with an average $\sigma_{\rm ELG} \simeq 0.101$ dex and $\sigma_{\rm LRG} \simeq 0.108$ dex. ELGs show lower metallicity at a given mass than LRGs for all but the highest masses. At $10^{9.5}$ M$_\odot$, the

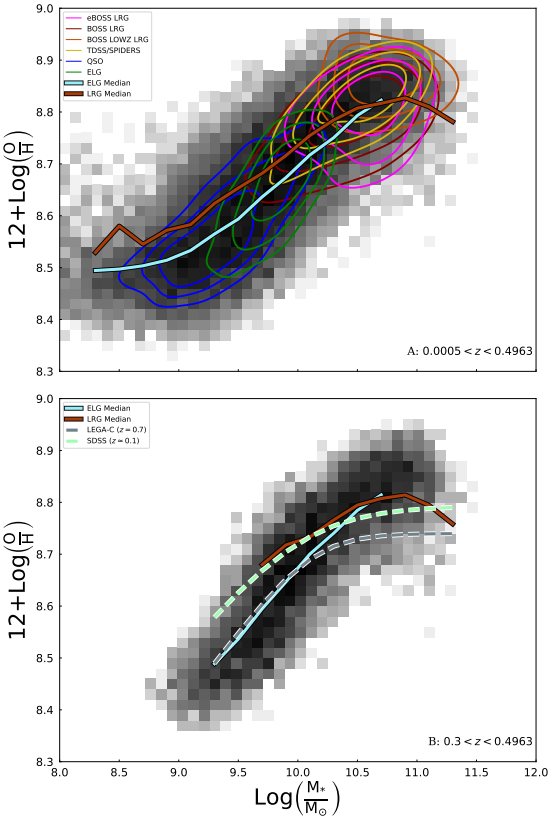


Figure 23. The mass–metallicity relation for eBOSS galaxies. This figure follows the plotting scheme of Fig. 22. Metallicities are determined using the empirical calibrations of K. Nakajima et al. (2022), which employ the R23 calibration and the O32 parameter to break the double-branching. **Panel A**: The data in the redshift range $0.0005 < z < 0.4963$ is shown in grayscale, with contours representing different target classes. **Panel B**: The data is trimmed to the redshift range $0.3 < z < 0.4963$ to limit the redshift evolution and remove cases of H II regions classified as galaxies (see §2.5). In both panels, the rust-red solid lines denote the medians for LRG and TDSS/SPIDERS spectra, whereas the light-blue solid lines denote the medians for ELG and QSO spectra. For comparison, we plot the MZR found in LEGA-C for $z \sim 0.7$ by Z. J. Lewis et al. (2024) in a gray dashed line and the SDSS-I MZR at $z \simeq 0.1$ found by M. Curti et al. (2020) in a green dashed line. The differences in trends between LRGs and ELGS highlight the importance of sample selection.

metallicity difference is 0.06 dex, highlighting the importance of sample selection.

For Panel B we trimmed the sample further to the redshift range $0.3 < z < 0.4963$ resulting in 13,866 spectra. This was done to avoid cases of H II regions classified as galaxies (see §2.5), which cause the metal-rich but low-mass outliers seen in Panel A. (These galaxies have artificially low stellar masses due to deblending problems in the Legacy Survey photometry see §2.5.) Another benefit of the trim was the ability to restrict the redshift evolution of the MZR, which is a major source of the scatter in Panel A. As seen in Panel B, the correlation of the MZRs is tighter in this redshift range with an average $\sigma_{\rm ELG} \simeq 0.09$ dex and $\sigma_{\rm LRG} \simeq 0.101$ dex.

For comparison, in Figure 23 panel B we plot the median MZR of the SDSS-I sample ($z \simeq 0.1$) found by M. Curti et al. (2020) and the median MZR of the LEGA-C survey ($z = 0.7$) found by Z. J. Lewis et al. (2024). The LEGA-C sample is K-band selected and relatively mass-complete (A. van der Wel et al. 2016). Both samples use very similar metallcity measurements to ours, mitigating strong line abundance calibration systematics. Given the redshift of the eBOSS sample used in this comparison ($z \sim 0.4$), we expect the median MZR of the ELGs and LRGs to lie between those of the SDSS-I ($z \sim 0.1$) and LEGA-C ($z \sim 0.7$) samples. However, this is not what we find. The LRGs show a fairly good match to the SDSS-I MZR over most of the mass range with a slightly elevated metallicity at $\log(M_*) = 10.5 - 11$. The LRGs were selected for their large 4000-Å breaks and red colors, a selection which favors older and dustier star-forming galaxies. Both stellar population age and dust attenuation may have residual correlations with metallicity, accounting for the fact that $z \sim 0.4$ eBOSS LRGs have an MZR more similar to $z \sim 0.1$ galaxies. In contrast, the eBOSS ELG MZR matches that of the $z \sim 0.7$ LEGA-C sample until about 10^{10} $M_\odot$ after which the median metallicity becomes higher than that of LEGA-C and even exceeds the median metallicity of SDSS-I galaxies in the most massive bin. The ELGs were selected based on their blue colors, which may be linked with less dust and metals and higher rates of star formation due to recent gas inflows, causing them to better match the MZR of high-redshift galaxies. The higher metallicities seen above $\log(M_*)$ are more difficult to explain and may have to do with survey volume differences between LEGA-C and eBOSS. In any case, the impact of sample selection effects on the MZR is evident. A more thorough Analysis of these differences will be the subject of future work.

4.3.5. *$H\delta_A$ vs Dn4000*

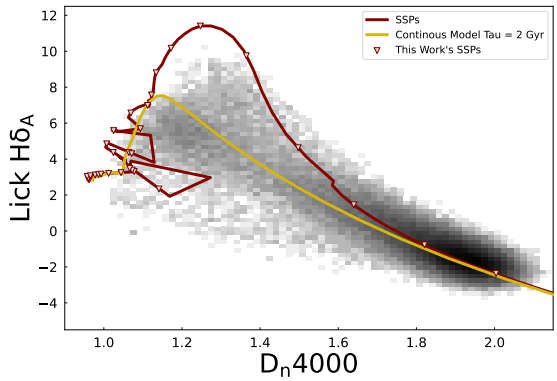


Figure 24. A spectral index diagram of $H\delta_A$ vs Dn4000. Spectra that pass the $H\delta_A$ error < 0.8 and Dn4000 error < 0.03 cuts from G. Kauffmann et al. (2003) (approximately 3.3% of the sample) are shown as a 2D log-scaled histogram (grayscale). Overplotted is an evolutionary sequence for a continuous star formation sequence (yellow) as well as a simple stellar population (dark red). The red triangles denote the exact values of the solar-metallicity SSPs used in this work.

Our final example is the $H\delta_A$ versus Dn4000 spectral indices plot (Fig. 24). To start, we applied the cuts

found in G. Kauffmann et al. (2003) of Hδ_a error < 0.8 and Dn4000 error < 0.03. We then removed spectra with unphysical index values and limited the redshift to $0.05 < z < 0.8$, resulting in 65,184 spectra or merely $\sim 3.4\%$ of our full sample. The majority of eBOSS galaxies have stellar continua that are too low S/N for the line indices to be measured accurately.

By comparing the Dn4000 and Hδ_A indices, we gain insight into the average stellar populations of this relatively bright sub-sample of eBOSS galaxies. Dn4000 traces the 4000-Å break and indicates the mean age of the stellar population; a low Dn4000 value suggests a young stellar population, while a high Dn4000 value indicates older stars. The Hδ_A index traces the strength of stellar Balmer absorption, which peaks at ages of a few 100 Myr, when A-stars dominate the spectrum.

In Figure 24, we overplot the Dn4000 and Hδ_a values of two C3K stellar population models: Solar metallicity SSPs and a continuous star formation model in red and yellow, respectively. A continuous star formation history model is a good match to the bulk of our data, but some galaxies with extreme Balmer absorption lie closer to the SSP models; such galaxies are likely post-starburst galaxies (K. D. French 2021). Many of the galaxies that lie well below the continuous models appear to be blazars: early-type galaxies with an additional power law continuum contribution arising from a relativistically beamed jet.

5. DATA USE RECOMMENDATIONS

We include a *Recommended Usage Guidelines* table (see Table 2) that summarizes best practices for the scientific use of the eBOSS-DAP catalog. While specific science goals may demand more specialized criteria, these recommendations offer a general foundation for reliable use of the catalog.

6. SUMMARY

This work presents the initial release and analysis of data and software products from the eBOSS Data Analysis Pipeline (eBOSS-DAP), designed to extend the utility of spectral data from the Extended Baryon Oscillation Spectroscopic Survey (eBOSS; K. S. Dawson et al. 2016). Previously, these data had primarily been utilized for measuring cosmological parameters. By using the eBOSS-DAP, we were able to extend the functionality of the survey and robustly characterize the eBOSS sample. Our main findings are as follows:

1. We characterized the eBOSS galaxy sample which includes galaxies targeted using a variety of color-based target selection algorithms (See §2). There are 1,901,834 spectra with 197,521 duplicates (1,704,313 unique galaxies) with a range of $z = 0$ to $z = 1.12$ (Fig. 1) and an average of 52% of their light down the fiber (Fig. 4). These spectra have an average S/N that peaks at S/N = 1.88 with an extended tail towards higher values (Fig. 2). We grouped the galaxies into 6 classes based on their target selection. The properties of these target classes are elucidated in Figures 3 and 20 – 23.

2. We made extensive use of the duplicate spectra to characterize the eBOSS survey's spectrophotometric calibration (§2.4). We show that spectrophotometry errors are strongly wavelength-dependent. For most eBOSS galaxies, relative flux calibration error is less than 10% between 4488 – 8397 Å with errors exceeding 50% at wavelengths less than 3665 Å or greater than 10283 Å (Fig. 6)

3. We provide a pipeline overview in which we detail how the MaNGA-DAP was modified to become the eBOSS-DAP (§3). The eBOSS-DAP utilizes algorithms from the MaNGA-DAP to process one-dimensional galaxy spectra from the eBOSS dataset, extracting comprehensive emission line fluxes, kinematics, continuum spectral indices, and spectral template weights. Like the MaNGA-DAP, the eBOSS-DAP can be easily adapted to work on datasets beyond eBOSS. Some key features of the eBOSS-DAP include: flexibility in adjusting emission line lists, spectral indices, and stellar templates, and tools for modifying fits, such as tying emission line parameters for improved precision.

4. Our final data products include emission line flux measurements (Fig. 13), spectral index measurements (Fig. 14), kinematics, and best-fit continuum models. We create three catalogs: a full sample (1,899,553 spectra) emission line catalog with a reduced emission line list (27 lines), a high equivalent width sample (167,466 spectra) emission line catalog which makes use of the full line list (80 lines), and a catalog of the spectral indices and the weights of the stellar continuum templates. In addition, we store the stellar continuum and emission-line fits for each spectrum as FITS files. All of these data products, as well as a suite of tools including the eBOSS-DAP source code, are publicly available. (See Data Availability for details.)

5. We provide catalog validation metrics, such as comparisons of emission-line fluxes in repeat spectra (Figures 17 and 18) and comparisons with fluxes measured by the SDSS pipeline (A. S. Bolton et al. 2012) (Fig. 16). Generally, we find the expected level of agreement between the fluxes given the errors, except at high S/N, where the spectrophotometric error becomes dominant. We provide average correction terms for a few commonly used lines and line ratios to approximately account for the spectrophotometric error (Table 1).

6. We use the eBOSS-DAP data to construct various galaxy scaling relations (Figures 20 - 24), highlighting the 6 target classes. We caution users of the data to account for sample selection effects when pursuing scientific applications.

Table 2: Recommended Usage Guidelines for the eBOSS-DAP Catalog

Category	**Recommended Regime**	**Notes**
Wavelength Coverage	3800–10200 Å (observed frame)	Spectrophotometry better than 25% is achieved in this range for most galaxies (see Fig. 6 and §2.4 for details.)
Emission Line Fluxes	S/N $\geq$ 3 for lines with $\lambda_{\rm observed} >$ 4500 Å; S/N $\geq$ 5 for lines with $\lambda_{\rm observed} \leq$ 4500 Å.	The higher threshold in the blue reflects an increased rate of spurious detections at these wavelengths. If using absolute flux values or ratios of lines widely separated in wavelength, it will be important to account for spectrophotometric error using the numbers given in Table 1. Emission lines have been corrected for foreground Milky Way reddening (see §3.2.)
Global Galaxy Quantities (e.g., a SFR based on $L_{H\alpha}$)	Require the fraction of light in the fiber to be $\gtrsim$ 25% and apply aperture corrections	The eBOSS spectra are obtained through 2″ diameter fibers that do not typically encompass the entire galaxy (see §2.3 and Fig. 4). The fraction of light in the fiber has been computed from the ratio of the *i*-band flux synthesized from spectrum and the *i*-band photometry and stored under the heading `infiber` in the `eboss_dap_auxdata` file. Note that for low S/N spectra, this quantity may be noisy.
High EW Emission Lines	EW< 100 Å or $\sigma_{line} \gtrsim$ 100 km s^{-1}	Very high EW narrow emission lines (such as Hα and [O III] in starbursting dwarf galaxies) are sometimes flagged as bad and clipped off by the `IDLSpec2D` pipeline (see §2.5 and Fig. 9.) Some of these clipped lines will have erroneous line fluxes reported in the eBOSS-DAP catalog. Techniques for identifying problem cases and a method to recover the clipped lines are briefly discussed in §2.5.
Emission Line Velocity Dispersions	Dispersion error < 50 km s^{-1}; values of −999.0 indicate the dispersion was not fit successfully	The reported emission line velocity dispersions have been corrected for instrumental resolution as follows: $\sigma = \sqrt{\sigma^2_{\rm raw} - \sigma^2_{\rm corr}}$ where $\sigma_{\rm raw}$ is the measured Gaussian line width and $\sigma_{\rm corr}$ is the instrumental resolution at line center. The instrumental resolution ranges from ∼40 - 80 km s^{-1}; line widths below this will have large measurement errors. In cases where $\sigma_{\rm raw} < \sigma_{\rm corr}$, the reported value is set to $\sigma = 0$ km s^{-1}. Line widths of all the emission lines are tied together during the fit with a 75% variation allowed (see §3.2.3).
Stellar Velocity Dispersion	Dispersion error < 50 km s^{-1}; values of −999.0 indicate the dispersion was invalid or exceeded 450 km s^{-1}	The eBOSS-DAP applies the same instrumental resolution correction described above (for the difference between the BOSS spectrograph and the CKC SSP template resolution) and reports the corrected value. Corrected values at or above 450 km s^{-1} are considered non-physical and are set to −999.0. Velocity dispersion values below the instrumental resolution ($\sigma_* \lesssim$ 60 km s^{-1}) will have large errors. In cases where $\sigma_{*,\rm raw} < \sigma_{*,\rm corr}$, the reported value is set to $\sigma_* = 0$ km s^{-1}. Repeat spectra suggest that the velocity dispersion errors are slightly underestimated (see Fig. 19). Scale uncertainties as suggested in Table 1.
Absorption Line Indices	Apply an error cut appropriate to the index of interest (e.g., D_n4000 error < 0.03 and Hδ_A error < 0.8)	Line indices have been measured from the data at its native resolution – i.e., they have not been corrected to a fiducial resolution (such as the original Lick resolution of 8.4 Å), nor are correction factors provided. Only a small fraction of the eBOSS sample has sufficient continuum S/N for reliable index measurements; for example, the suggested D_n4000/Hδ_A cuts retain only ∼3.4% of the full sample (see §4.3.5). Beware of selection effects induced by S/N cuts.
Photometry	$z > 0.1$	Below this redshift, galaxy deblending by both the SDSS and the Legacy Survey photometric pipelines can be unreliable, leading to errors in the photometric data (i.e., H II regions can be classified as separate galaxies; see §2.5 and Fig. 8, for an example). This can also cause strong aperture bias. At lower redshifts, visual inspection of the photometry may be required.
Additional Quality Flags	`FIBERMASKED = F` [...]_ERR > 0	As described in §3.2.1, we have retained some mask bits set by the `IDLSpec2d` pipeline in the `fibermasked` field in the `eboss_dap_auxdata` file. These mask bits signal potential problems with the flatfield, arc, or trace, although most of the spectra appear to be of good quality. The small faction of galaxies with `fibermasked = T` should be removed for a maximally conservative analysis. Error values set to -999 on any measured quantity indicate a problem with the measurement.
Galaxy scaling relations and other population studies	Consider target selection effects Remove duplicate spectra	SDSS-IV contains several different galaxy surveys with distinct target selection algorithms (see §2 and Appendix A). Target selection can have significant systematic effects on galaxy scaling relations; for example, see the mass-metallicity relation in Fig. 23. Targeting information can be found in the `target_class` and `target_text` fields in the `eboss_dap_auxdata` file as well as in the SDSS `spAll` file. Roughly 10% of the eBOSS spectra are duplicates. To retain only the highest quality spectrum of each galaxy, select on `SPECPRIMARY = 1` in the `eboss_dap_auxdata` file.

7. We provide a table that contains Recommended Usage Guidelines for the eBOSS-DAP catalog (§5). These guidelines summarize the key caveats discussed throughout this paper, providing a starting point for the appropriate use of the catalog. Individual science cases will have their own specific requirements beyond these general guidelines.

In summary, we have produced an extensive set of well-characterized emission line measurements for the 1.7 million galaxies in the eBOSS sample. This data will be useful for a variety of statistical studies of galaxy evolution at $z < 1$. The eBOSS-DAP catalogs will be of particular value for AGN studies due to the sample makeup and the expanded line list. In Matthews Acuña et al, in prep, we focus on utilizing the high quantity of [Ne V] 3347, 3427 detections to study coronal line detections in AGN.

ACKNOWLEDGMENTS

The authors thank the anonymous referee for their constructive comments which have signficantly improved the paper. OMA, CAT, and DM gratefully acknowledge support for this work from NSF grant AST-2107725. OMA thanks I. McConachie, I. Laseter, and M. Maseda for helpful comments. AD-S gratefully acknowledges support for this work from NSF grant 2107726. BL gratefully acknowledges support for this work from NSF grant 2107727. ZJL acknowledges support from the National Science Foundation Graduate Research Fellowship under grant No. 2137424.

This research uses services or data provided by the Astro Data Lab at NSF's NOIRLab. NOIRLab is operated by the Association of Universities for Research in Astronomy (AURA), Inc. under a cooperative agreement with the National Science Foundation.

Funding for the Sloan Digital Sky Survey IV has been provided by the Alfred P. Sloan Foundation, the U.S.Department of Energy Office of Science, and the Participating Institutions. SDSS-IV acknowledges support and resources from the Center for High-Performance Computing at the University of Utah. The SDSS website is available at **www.sdss.org**. SDSS-IV is managed by the Astrophysical Research Consortium for the Participating Institutions of the SDSS Collaboration including the Brazilian Participation Group, the Carnegie Institution for Science, Carnegie Mellon University, the Chilean Participation Group, the French Participation Group, Harvard-Smithsonian Center for Astrophysics, Instituto de Astrofísica de Canarias, The Johns Hopkins University, Kavli Institute for the Physics and Mathematics of the Universe (IPMU)/University of Tokyo, Lawrence Berkeley National Laboratory, Leibniz Institut für Astrophysik Potsdam (AIP), Max-Planck-Institut für Astronomie (MPIA Heidelberg), MaxPlanck-Institut für Astrophysik (MPA Garching), Max-PlanckInstitut für Extraterrestrische Physik (MPE), National Astronomical Observatories of China, New Mexico State University,New York University, University of Notre Dame, Observatário Nacional/MCTI, The Ohio State University, Pennsylvania State University, Shanghai Astronomical Observatory, United Kingdom Participation Group, Universidad Nacional Autónoma de México, University of Arizona, University of Colorado Boulder, University of Oxford, University of Portsmouth, University of Utah, University of Virginia, University of Washington, University of Wisconsin, Vanderbilt University, and Yale University.

SOFTWARE

This research made use of `Astropy`, a community-developed core Python package for Astronomy (Astropy Collaboration et al. 2013, 2018, 2022); `dust-extinction` (K. D. Gordon 2024); `dustmaps` (G. Green 2018); `FSPS` (C. Conroy et al. 2009; C. Conroy & J. E. Gunn 2010) and its Python bindings package `Python-FSPS`[12]; `IPython` (F. Pérez & B. E. Granger 2007); `MaNGA-DAP` (K. B. Westfall et al. 2019; F. Belfiore et al. 2019); `matplotlib` (J. D. Hunter 2007); `numpy` (C. R. Harris et al. 2020); `pandas` (The pandas development team 2020; Wes McKinney 2010); `SciPy` (P. Virtanen et al. 2020); and `Seaborn` (M. L. Waskom 2021)

Additionally, computing resources from the University of Wisconsin–Madison Center for High Throughput Computing (Center for High Throughput Computing 2006) were used to run the pipeline.

DATA AVAILABILITY

All catalogs in this paper are available at https://datalab.noirlab.edu/data/sdss#sdss-iv-eboss-dap-value-added-catalog.

The `eBOSS-DAP` is available at https://github.com/owenmatthewsa/ebossdap. Summary tables of figures 6, 16,17, and 18 are available at this same location in addition to tables used in 3.2.3. The data used in additional plots within this article are available upon request. All fits reported in this paper or in the catalog can be reproduced for any galaxy by running the eBOSS-DAP code on the original spectra.

REFERENCES

Abazajian, K., Adelman-McCarthy, J. K., Agüeros, M. A., et al. 2004 AJ, 128, 502, doi: 10.1086/421365
Abazajian, K. N., Adelman-McCarthy, J. K., Agüeros, M. A., et al. 2009 ApJS, 182, 543, doi: 10.1088/0067-0049/182/2/543
Abdurro'uf, Accetta, K., Aerts, C., et al. 2022 ApJS, 259, 35, doi: 10.3847/1538-4365/ac4414
Anand, A., Nelson, D., & Kauffmann, G. 2021 MNRAS, 504, 65, doi: 10.1093/mnras/stab871
Andrews, B. H., & Martini, P. 2013 ApJ, 765, 140, doi: 10.1088/0004-637X/765/2/140
Asa'd, R., Coelho, P. R. T., John, J. M., et al. 2025 AJ, 170, 85, doi: 10.3847/1538-3881/addaad
Astropy Collaboration, Robitaille, T. P., Tollerud, E. J., et al. 2013 A&A, 558, A33, doi: 10.1051/0004-6361/201322068
Astropy Collaboration, Price-Whelan, A. M., Sipőcz, B. M., et al. 2018 AJ, 156, 123, doi: 10.3847/1538-3881/aabc4f
Astropy Collaboration, Price-Whelan, A. M., Lim, P. L., et al. 2022 ApJ, 935, 167, doi: 10.3847/1538-4357/ac7c74
Baldwin, J. A., Phillips, M. M., & Terlevich, R. 1981 PASP, 93, 5, doi: 10.1086/130766

[12] https://github.com/dfm/python-fsps

Belfiore, F., Maiolino, R., Maraston, C., et al. 2016 MNRAS, 461, 3111, doi: 10.1093/mnras/stw1234
Belfiore, F., Westfall, K. B., Schaefer, A., et al. 2019 AJ, 158, 160, doi: 10.3847/1538-3881/ab3e4e
Blanton, M. R., & Moustakas, J. 2009 ARA&A, 47, 159, doi: 10.1146/annurev-astro-082708-101734
Blanton, M. R., Bershady, M. A., Abolfathi, B., et al. 2017 AJ, 154, 28, doi: 10.3847/1538-3881/aa7567
Bolton, A. S., Schlegel, D. J., Aubourg, É., et al. 2012 AJ, 144, 144, doi: 10.1088/0004-6256/144/5/144
Boquien, M., Burgarella, D., Roehlly, Y., et al. 2019 A&A, 622, A103, doi: 10.1051/0004-6361/201834156
Brinchmann, J., Charlot, S., Heckman, T. M., et al. 2004, Stellar masses, star formation rates, metallicities and AGN properties for 200,000 galaxies in the SDSS Data Release Two (DR2), https://arxiv.org/abs/astro-ph/0406220
Bruzual, G., & Charlot, S. 2003 MNRAS, 344, 1000, doi: 10.1046/j.1365-8711.2003.06897.x
Bundy, K., Bershady, M. A., Law, D. R., et al. 2015 ApJ, 798, 7, doi: 10.1088/0004-637X/798/1/7
Byler, N., Dalcanton, J. J., Conroy, C., & Johnson, B. D. 2017 ApJ, 840, 44, doi: 10.3847/1538-4357/aa6c66
Byrne, C. M., & Stanway, E. R. 2023 MNRAS, 521, 4995, doi: 10.1093/mnras/stad832
Calzetti, D., Armus, L., Bohlin, R. C., et al. 2000 ApJ, 533, 682, doi: 10.1086/308692
Cappellari, M. 2012, pPXF: Penalized Pixel-Fitting stellar kinematics extraction,, Astrophysics Source Code Library, record ascl:1210.002
Cappellari, M. 2023 MNRAS, 526, 3273, doi: 10.1093/mnras/stad2597
Castelli, F. 2005 Memorie della Societa Astronomica Italiana Supplementi, 8, 25
Center for High Throughput Computing. 2006, Center for High Throughput Computing, Center for High Throughput Computing, doi: 10.21231/GNT1-HW21
Chabrier, G. 2003 PASP, 115, 763, doi: 10.1086/376392
Chiang, Y.-K. 2023 ApJ, 958, 118, doi: 10.3847/1538-4357/acf4a1
Choi, J., Dotter, A., Conroy, C., et al. 2016 ApJ, 823, 102, doi: 10.3847/0004-637X/823/2/102
Clerc, N., Merloni, A., Zhang, Y. Y., et al. 2016 MNRAS, 463, 4490, doi: 10.1093/mnras/stw2214
Cleri, N. J., Olivier, G. M., Backhaus, B. E., et al. 2025 arXiv e-prints, arXiv:2506.21660, doi: 10.48550/arXiv.2506.21660
Coelho, P. R. T., Bruzual, G., & Charlot, S. 2020 MNRAS, 491, 2025, doi: 10.1093/mnras/stz3023
Conroy, C. 2013 ARA&A, 51, 393, doi: 10.1146/annurev-astro-082812-141017
Conroy, C., & Gunn, J. E. 2010 ApJ, 712, 833, doi: 10.1088/0004-637X/712/2/833
Conroy, C., Gunn, J. E., & White, M. 2009 ApJ, 699, 486, doi: 10.1088/0004-637X/699/1/486
Curti, M., Mannucci, F., Cresci, G., & Maiolino, R. 2020 MNRAS, 491, 944, doi: 10.1093/mnras/stz2910
Dawson, K. S., Schlegel, D. J., Ahn, C. P., et al. 2013 AJ, 145, 10, doi: 10.1088/0004-6256/145/1/10
Dawson, K. S., Kneib, J.-P., Percival, W. J., et al. 2016 AJ, 151, 44, doi: 10.3847/0004-6256/151/2/44
Dey, A., Schlegel, D. J., Lang, D., et al. 2019 AJ, 157, 168, doi: 10.3847/1538-3881/ab089d
Dotter, A. 2016 ApJS, 222, 8, doi: 10.3847/0067-0049/222/1/8
Draine, B. T., Aniano, G., Krause, O., et al. 2014 ApJ, 780, 172, doi: 10.1088/0004-637X/780/2/172
Dwelly, T., Salvato, M., Merloni, A., et al. 2017 MNRAS, 469, 1065, doi: 10.1093/mnras/stx864
Eisenstein, D. J., Annis, J., Gunn, J. E., et al. 2001 AJ, 122, 2267, doi: 10.1086/323717
Eisenstein, D. J., Zehavi, I., Hogg, D. W., et al. 2005 ApJ, 633, 560, doi: 10.1086/466512
Eisenstein, D. J., Weinberg, D. H., Agol, E., et al. 2011 AJ, 142, 72, doi: 10.1088/0004-6256/142/3/72
Filippenko, A. V. 1982 PASP, 94, 715, doi: 10.1086/131052
Fitzpatrick, M. J., Olsen, K., Economou, F., et al. 2014, in Society of Photo-Optical Instrumentation Engineers (SPIE) Conference Series, Vol. 9149, Observatory Operations: Strategies, Processes, and Systems V, ed. A. B. Peck, C. R. Benn, & R. L. Seaman, 91491T, doi: 10.1117/12.2057445
French, K. D. 2021 PASP, 133, 072001, doi: 10.1088/1538-3873/ac0a59
Fukugita, M., Ichikawa, T., Gunn, J. E., et al. 1996 AJ, 111, 1748, doi: 10.1086/117915
Geller, M. J., Dell'Antonio, I. P., Kurtz, M. J., et al. 2005 ApJL, 635, L125, doi: 10.1086/499399
Geller, M. J., Hwang, H. S., Dell'Antonio, I. P., et al. 2016 ApJS, 224, 11, doi: 10.3847/0067-0049/224/1/11
Geller, M. J., Hwang, H. S., Fabricant, D. G., et al. 2014 ApJS, 213, 35, doi: 10.1088/0067-0049/213/2/35
Gordon, K. D. 2024 Journal of Open Source Software, 9, 7023, doi: 10.21105/joss.07023
Gordon, K. D., Cartledge, S., & Clayton, G. C. 2009 ApJ, 705, 1320, doi: 10.1088/0004-637X/705/2/1320
Green, G. 2018 The Journal of Open Source Software, 3, 695, doi: 10.21105/joss.00695
Gunn, J. E., Carr, M., Rockosi, C., et al. 1998 AJ, 116, 3040, doi: 10.1086/300645
Gunn, J. E., Siegmund, W. A., Mannery, E. J., et al. 2006 AJ, 131, 2332, doi: 10.1086/500975
Harris, C. R., Millman, K. J., van der Walt, S. J., et al. 2020 Nature, 585, 357, doi: 10.1038/s41586-020-2649-2
Heckman, T. M., Kauffmann, G., Brinchmann, J., et al. 2004 ApJ, 613, 109, doi: 10.1086/422872
Huang, C., Zou, H., Kong, X., et al. 2019 ApJ, 886, 31, doi: 10.3847/1538-4357/ab4902
Hunter, J. D. 2007 Computing in Science & Engineering, 9, 90, doi: 10.1109/MCSE.2007.55
Ji, X., & Yan, R. 2022 A&A, 659, A112, doi: 10.1051/0004-6361/202142312
Juneau, S., Bournaud, F., Charlot, S., et al. 2014 ApJ, 788, 88, doi: 10.1088/0004-637X/788/1/88
Kauffmann, G., White, S. D. M., Heckman, T. M., et al. 2004 Monthly Notices of the Royal Astronomical Society, 353, 713, doi: 10.1111/j.1365-2966.2004.08117.x
Kauffmann, G., Heckman, T. M., White, S. D. M., et al. 2003 MNRAS, 341, 33, doi: 10.1046/j.1365-8711.2003.06291.x
Kennicutt, R. C., & Evans, N. J. 2012 ARA&A, 50, 531, doi: 10.1146/annurev-astro-081811-125610
Kewley, L. J., Dopita, M. A., Leitherer, C., et al. 2013 ApJ, 774, 100, doi: 10.1088/0004-637X/774/2/100
Kewley, L. J., & Ellison, S. L. 2008 ApJ, 681, 1183, doi: 10.1086/587500
Kewley, L. J., Groves, B., Kauffmann, G., & Heckman, T. 2006 MNRAS, 372, 961, doi: 10.1111/j.1365-2966.2006.10859.x
Kewley, L. J., Nicholls, D. C., & Sutherland, R. S. 2019 ARA&A, 57, 511, doi: 10.1146/annurev-astro-081817-051832
Kurucz, R. L. 1970 SAO Special Report, 309
Kurucz, R. L. 1993, SYNTHE spectrum synthesis programs and line data
Lan, T.-W., & Mo, H. 2018 ApJ, 866, 36, doi: 10.3847/1538-4357/aadc08
Law, D. R., Westfall, K. B., Bershady, M. A., et al. 2021a AJ, 161, 52, doi: 10.3847/1538-3881/abcaa2
Law, D. R., Ji, X., Belfiore, F., et al. 2021b ApJ, 915, 35, doi: 10.3847/1538-4357/abfe0a
Lewis, Z. J., Andrews, B. H., Bezanson, R., et al. 2024 ApJ, 964, 59, doi: 10.3847/1538-4357/ad250c
Lupton, R., Gunn, J. E., Ivezić, Z., Knapp, G. R., & Kent, S. 2001, in Astronomical Society of the Pacific Conference Series, Vol. 238, Astronomical Data Analysis Software and Systems X, ed. J. Harnden, F. R., F. A. Primini, & H. E. Payne, 269, doi: 10.48550/arXiv.astro-ph/0101420
MacLeod, C. L., Green, P. J., Anderson, S. F., et al. 2018 AJ, 155, 6, doi: 10.3847/1538-3881/aa99da
Mannucci, F., Cresci, G., Maiolino, R., Marconi, A., & Gnerucci, A. 2010 MNRAS, 408, 2115, doi: 10.1111/j.1365-2966.2010.17291.x
Maraston, C., & Strömbäck, G. 2011 MNRAS, 418, 2785, doi: 10.1111/j.1365-2966.2011.19738.x
Morganson, E., Green, P. J., Anderson, S. F., et al. 2015 ApJ, 806, 244, doi: 10.1088/0004-637X/806/2/244

Morrison, S., Ibarra-Medel, H. J., Holtzman, J., et al. 2026 ApJ (submitted)
Myers, A. D., Palanque-Delabrouille, N., Prakash, A., et al. 2015 The Astrophysical Journal Supplement Series, 221, 27, doi: 10.1088/0067-0049/221/2/27
Nakajima, K., Ouchi, M., Xu, Y., et al. 2022 ApJS, 262, 3, doi: 10.3847/1538-4365/ac7710
Nikutta, R., Fitzpatrick, M., Scott, A., & Weaver, B. 2020 Astronomy and Computing, 33, 100411, doi: https://doi.org/10.1016/j.ascom.2020.100411
O'Donnell, J. E. 1994 ApJ, 422, 158, doi: 10.1086/173713
Oke, J. B. 1990 AJ, 99, 1621, doi: 10.1086/115444
Peng, Y.-j., Lilly, S. J., Kovač, K., et al. 2010 ApJ, 721, 193, doi: 10.1088/0004-637X/721/1/193
Pérez, F., & Granger, B. E. 2007 Computing in Science and Engineering, 9, 21, doi: 10.1109/MCSE.2007.53
Popesso, P., Concas, A., Cresci, G., et al. 2023 MNRAS, 519, 1526, doi: 10.1093/mnras/stac3214
Prakash, A., Licquia, T. C., Newman, J. A., et al. 2016 The Astrophysical Journal Supplement Series, 224, 34, doi: 10.3847/0067-0049/224/2/34
Prugniel, P., & Soubiran, C. 2001 A&A, 369, 1048, doi: 10.1051/0004-6361:20010163
Raichoor, A., Comparat, J., Delubac, T., et al. 2017 MNRAS, 471, 3955, doi: 10.1093/mnras/stx1790
Raichoor, A., de Mattia, A., Ross, A. J., et al. 2021 MNRAS, 500, 3254, doi: 10.1093/mnras/staa3336
Reid, B., Ho, S., Padmanabhan, N., et al. 2016 MNRAS, 455, 1553, doi: 10.1093/mnras/stv2382
Salim, S., Lee, J. C., Ly, C., et al. 2014 ApJ, 797, 126, doi: 10.1088/0004-637X/797/2/126
Scholte, D., Saintonge, A., Moustakas, J., et al. 2024 MNRAS, 535, 2341, doi: 10.1093/mnras/stae2477
Smee, S. A., Gunn, J. E., Uomoto, A., et al. 2013 AJ, 146, 32, doi: 10.1088/0004-6256/146/2/32
Stoughton, C., Lupton, R. H., Bernardi, M., et al. 2002 AJ, 123, 485, doi: 10.1086/324741
Strauss, M. A., Weinberg, D. H., Lupton, R. H., et al. 2002 AJ, 124, 1810, doi: 10.1086/342343
The pandas development team. 2020, pandas-dev/pandas: Pandas,, latest Zenodo, doi: 10.5281/zenodo.3509134
Tremonti, C. A., Heckman, T. M., Kauffmann, G., et al. 2004 ApJ, 613, 898, doi: 10.1086/423264
van der Wel, A., Noeske, K., Bezanson, R., et al. 2016 ApJS, 223, 29, doi: 10.3847/0067-0049/223/2/29
Virtanen, P., Gommers, R., Oliphant, T. E., et al. 2020 Nature Methods, 17, 261, doi: 10.1038/s41592-019-0686-2
Wang, B., Leja, J., de Graaff, A., et al. 2024 ApJL, 969, L13, doi: 10.3847/2041-8213/ad55f7
Waskom, M. L. 2021 Journal of Open Source Software, 6, 3021, doi: 10.21105/joss.03021
Weinmann, S. M., van den Bosch, F. C., Yang, X., & Mo, H. J. 2006 MNRAS, 366, 2, doi: 10.1111/j.1365-2966.2005.09865.x
Wes McKinney. 2010, in Proceedings of the 9th Python in Science Conference, ed. Stéfan van der Walt & Jarrod Millman, 56 – 61, doi: 10.25080/Majora-92bf1922-00a
Westfall, K. B., Cappellari, M., Bershady, M. A., et al. 2019 AJ, 158, 231, doi: 10.3847/1538-3881/ab44a2
Wright, E. L., Eisenhardt, P. R. M., Mainzer, A. K., et al. 2010 AJ, 140, 1868, doi: 10.1088/0004-6256/140/6/1868
York, D. G., Adelman, J., Anderson, John E., J., et al. 2000 AJ, 120, 1579, doi: 10.1086/301513
Zahid, H. J., Dima, G. I., Kudritzki, R.-P., et al. 2014 ApJ, 791, 130, doi: 10.1088/0004-637X/791/2/130
Zahid, H. J., Geller, M. J., Fabricant, D. G., & Hwang, H. S. 2016 ApJ, 832, 203, doi: 10.3847/0004-637X/832/2/203
Zhu, G. B., Comparat, J., Kneib, J.-P., et al. 2015 ApJ, 815, 48, doi: 10.1088/0004-637X/815/1/48

APPENDIX

A. TARGET SELECTION

The BOSS and eBOSS surveys targeted galaxies and quasars for spectroscopy using a wide variety of algorithms (K. S. Dawson et al. 2013, 2016). Targeting information for each galaxy can be found in the the SDSS `spAll` file as hexidecimal target mask bits stored in `BOSS_TARGET1, ANCILLARY_TARGET1, ANCILLARY_TARGET2, EBOSS_TARGET0, EBOSS_TARGET1`, and `EBOSS_TARGET2`. We have translated the hexidecimal mask bits into text format and stored them in the `eBOSS_DAP_auxdata` table under the heading `'target_text'`. In total there are 595 unique target types. For convenience, we have grouped them into 8 broad 'target classes' which are defined in Table A1 and stored under the heading '`target_class`'. These target classes are shown as colored contours Figures 1 - 4 and 20 - 23 . Additional information on SDSS-IV target selection can be found at https://www.sdss4.org/dr17/spectro/targets/.

Table A1: Target Classes

Target Class Name (description)	**Number of Galaxies (% of sample)**	**Median Redshift**	**SDSS-IV Target Types Included**
QSO	61,300 (3.22%)	0.30	BLAZGRQSO, BLAZGXQSO, GAL_NEAR_QSO, KQSO_BOSS, QSO1_BAD_BOSS, QSO1_EBOSS_CORE, QSO1_EBOSS_FIRST, QSO1_PTF, QSO1_REOBS, QSO1_VAR_S82, QSO_BONUS, QSO_BONUS_MAIN, QSO_BOSS_TARGET, QSO_CORE, QSO_CORE_ED, QSO_CORE_LIKE, QSO_CORE_MAIN, QSO_DEEP, QSO_EBOSS_CORE, QSO_EBOSS_FIRST, QSO_EBOSS_KDE, QSO_EBOSS_W3_ADM, QSO_FIRST_BOSS, QSO_GRI, QSO_HIZ, QSO_KDE, QSO_KDE_COADD, QSO_KNOWN, QSO_KNOWN_MIDZ, QSO_LIKE, QSO_NN, QSO_PTF, QSO_RADIO, QSO_RIZ, QSO_SDSS_TARGET, QSO_SUPPZ, QSO_UKIDSS, QSO_VAR, QSO_VAR_FPG, QSO_VAR_LF, QSO_VAR_SDSS, QSO_WISE_FULL_SKY, QSO_WISE_SUPP, QSO_XD_KDE_PAIR, RADIO_2LOBE_QSO, TEMPLATE_QSO_SDSS1, WISE_BOSS_QSO
LRG3 (SDSS-III/BOSS Luminous Red Galaxies)	1,024,272 (53.86%)	0.54	GAL_CMASS, GAL_CMASS_ALL, GAL_CMASS_COMM, GAL_CMASS_SPARSE
LRG4 (SDSS-IV/eBOSS Luminous Red Galaxies)	200,368 (10.54%)	0.70	FAINT_HIZ_LRG, HIZ_LRG, LRG1_IDROP, LRG1_WISE, LRG_IZW, LRG_RIW, LRG_ROUND3
LRGL (BOSS low-z Luminous Red Galaxies)	369,507 (19.43%)	0.33	GAL_LOZ
ELG (Emission Line Galaxies)	180,025 (9.47%)	0.82	ELG, ELG1_EBOSS, ELG1_EXTENDED, ELG1_NGC, ELG1_SGC, ELG_DECALS_TEST1, ELG_DESI_TEST1, ELG_DES_TEST1, ELG_GRIW_TEST1, ELG_SCUSS_TEST1, ELG_SDSS_TEST1, ELG_TEST1, ELG_UGRIZW_TEST1, ELG_UGRIZWbright_TEST1, FAINT_ELG, SEQUELS_ELG, SEQUELS_ELG_LOWP
TDSP (TDSS and SPIDERS Targets)	37,594 (1.98%)	0.27	TDSS_A, TDSS_B, TDSS_CP, TDSS_FES_DE, TDSS_FES_HYPQSO, TDSS_FES_HYPSTAR, TDSS_FES_NQHISN, TDSS_FES_VARBAL, TDSS_PILOT, TDSS_PILOT_SNHOST, TDSS_RQS1, TDSS_RQS2, TDSS_RQS3, TDSS_RQS3v, TDSS_TARGET, SPIDERS_CODEX_CLUS_CFHT, SPIDERS_CODEX_CLUS_DECALS, SPIDERS_CODEX_CLUS_PS1, SPIDERS_PILOT, SPIDERS_RASS_AGN, SPIDERS_RASS_CLUS, SPIDERS_TARGET, SPIDERS_XCLASS_CLUS, SPIDERS_XMMSL_AGN, EFEDS_COSMOQSO, EFEDS_CSC2, EFEDS_EROSITA_AGN, EFEDS_EROSITA_CLUS, EFEDS_GAIAWISE_QSO, EFEDS_HSC_REDAGN, EFEDS_HSC_REDMAPPER, EFEDS_HSC_WERGS, EFEDS_KIDS_QSO, EFEDS_SDSSWISE_QSO, EFEDS_SDSS_REDMAPPER, EFEDS_WISE_AGN, EFEDS_WISE_VARAGN, EFEDS_XMMATLAS, S82X_BRIGHT_TARGET, S82X_GTRADMZ4_TARGET, S82X_LSSTZ4_TARGET, S82X_PETERS15_COLORVAR_TARGET, S82X_RICHARDS15_PHOTOQSO_TARGET, S82X_SACLAY_BDT_TARGET, S82X_SACLAY_HIZ_TARGET, S82X_SACLAY_VAR_TARGET, S82X_TILE1, S82X_TILE2, S82X_TILE3, S82X_UNWISE_TARGET, S82X_WISE_TARGET, S82X_XMM_TARGET
ANCI (Ancillary Targets)	28,310 (1.49%)	0.31	25ORI_WISE, 25ORI_WISE_W3, BLAZGRFLAT, BLAZGX, BLAZGXR, BLAZR, BLAZXR, BLUE_RADIO, BRIGHTGAL, CHANDRAV1, CLUSTER_MEMBER, CXOBRIGHT, CXOGRIZ, CXORED, ELAIS_N1_FIRST, ELAIS_N1_GMRT_GARN, ELAIS_N1_GMRT_TAYLOR, ELAIS_N1_JVLA, ELAIS_N1_LOFAR, FAINTERM, IAMASERS, KOE2023BSTAR, KOE2023_STAR, KOE2068BSTAR, KOE2068_STAR, KOEKAP_STAR, LBG, ODDBAL, OTBAL, PTF_GAL, RM_TILE1, RM_TILE2, RQSS_SF, RQSS_SFC, SEQUELS_PTF_VARIABLE, SEQUELS_TARGET, SN_GAL1, SN_GAL2, SN_GAL3, SN_LOC, SPEC_SN, SPOKE, STRIPE82BCG, TAU_STAR, VARBAL, VARS, WHITEDWARF_NEW, WHITEDWARF_SDSS, WISE_COMPLETE, XMMBRIGHT, XMMGRIZ, XMMHR, XMMRED, XMMSDSS, XMM_PRIME, XMM_SECOND
MISC (Other Targets)	458 (0.02%)	0.23	STD_FSTAR, TEMPLATE_GAL_PHOTO

B. LINE LIST

Table B1: Emission Line List

Name (* Unavailable in MaNGA; † Unavailable in SDSS)	Vacuum Wavelength	Flux Tie	Integration Range	Dispersion Tie A | B[13]	In Low EW Sample (Hβ EW < 10)
[C III] 1906*†	1906.680	-	1902.2 – 1907.6	[0.57 - 1.75] (Hα | Hβ)	No
[C III] 1909*	1908.734	-	1907.6 – 1914.7	[C III] 1906	No
[C II] 2325C*†	2326.113	-	2320.6 – 2326.4	[C II] 2325D	No
[C II] 2325D*†	2327.645	-	2326.4 – 2328.3	[0.57 - 1.75] (Hα | Hβ)	No
[C II] 2328*†	2328.838	-	2328.4 – 2331.8	[C II] 2325D	No
[Fe II*] 2365*†	2365.552	-	2361.9 – 2368.6	[Fe II*] 2396	No
[Fe II*] 2396*†	2396.350	-	2392.1 – 2400.1	[0.57 - 1.75] (Hα | Hβ)	No
[Ne IV] 2423*†	2422.560	-	2417.1 – 2424.2	[Ne IV] 2425	No
[Ne IV] 2425*†	2425.140	-	2424.2 – 2430.2	[0.57 - 1.75] (Hα | Hβ)	No
[O II] 2470*†	2471.027	-	2467.5 – 2474.8	[0.57 - 1.75] (Hα | Hβ)	No
[Fe II*] 2613*†	2612.654	-	2608.7 – 2617.2	[0.57 - 1.75] (Hα | Hβ)	No
[Fe II*] 2626*†	2626.451	-	2622.2 – 2629.5	[Fe II*] 2613	No
[Fe II*] 2632*†	2632.110	-	2629.9 – 2635.4	[Fe II*] 2613	No
He II 2734*†	2733.700	-	2729.7 – 2737.7	[0.57 - 1.75] (Hα | Hβ)	No
[Mg V] 2784*†	2783.700	-	2780.2 – 2787.2	[0.57 - 1.75] (Hα | Hβ)	No
[Mg II] 2796*	2796.350	-	2787.9 – 2797.7	[S III] 9533	Yes
[Mg II] 2803*†	2803.531	-	2797.7 – 2809.8	[Mg II] 2796	Yes
[Fe IV] 2830*†	2830.300	-	2827.8 – 2832.8	[Fe IV] 2836	No
[Fe IV] 2836*†	2836.000	-	2832.8 – 2839.2	[0.57 - 1.75] (Hα | Hβ)	No
He I 2945*†	2945.103	-	2943.1 – 2949.1	[0.57 - 1.75] (Hα | Hβ)	No
[O III] 3134*†	3134.200	-	3126.0 – 3141.0	[0.57 - 1.75] (Hα | Hβ)	No
He I 3189*†	3188.670	-	3178.7 – 3196.0	[0.57 - 1.75] (Hα | Hβ)	No
He II 3204*†	3204.019	-	3195.1 – 3211.7	[0.57 - 1.75] (Hα | Hβ)	No
[Ne V] 3347*†	3346.783	0.366 * NeV_3427	3336.7 – 3355.0	[Ne V] 3427	Yes
[Ne V] 3427*†	3426.864	-	3415.7 – 3437.0	[0.57 - 1.75] (Hα | Hβ)	Yes
[Fe VII] 3586*†	3586.000	-	3576.0 – 3596.0	[0.57 - 1.75] (Hα | Hβ)	No
[O II] 3727	3727.092	-	3716.3 – 3738.3	[0.57 - 1.75] (Hα | Hβ)	Yes
[O II] 3729	3729.875	-	-1.0 – -1.0	[O II] 3727	Yes
H12†	3751.217	-	3746.2 – 3756.2	[0.57 - 1.75] (Hα | Hβ)	No
[Fe VII] 3760*†	3760.000	-	3756.6 – 3766.6	[0.57 - 1.75] (Hα | Hβ)	No
H11†	3771.701	-	3761.7 – 3781.7	[0.57 - 1.75] (Hα | Hβ)	No
Hθ†	3798.976	-	3789.0 – 3809.0	[0.57 - 1.75] (Hα | Hβ)	No
Hη†	3836.472	-	3826.5 – 3846.5	[0.57 - 1.75] (Hα | Hβ)	Yes
[Ne III] 3870	3869.860	-	3859.9 – 3879.9	[0.57 - 1.75] (Hα | Hβ)	Yes
He I 3890†	3889.749	-	-1.0 – -1.0	Hζ	No
Hζ†	3890.151	-	3880.2 – 3900.2	[0.57 - 1.75] (Hα | Hβ)	No
[Ne III] 3969	3968.590	0.30 * NeIII_3870	-1.0 – -1.0	[Ne III] 3870	Yes
Hϵ	3971.195	-	3961.2 – 3981.2	[0.57 - 1.75] (Hα | Hβ)	Yes
He I 4027*†	4027.175	-	4023.3 – 4031.1	[0.57 - 1.75] (Hα | Hβ)	No
[S II] 4070*†	4069.750	-	4063.0 – 4076.0	[0.57 - 1.75] (Hα | Hβ)	No
Hδ	4102.892	-	4092.9 – 4112.9	[0.57 - 1.75] (Hα | Hβ)	Yes
Hγ	4341.684	-	4331.7 – 4351.7	[0.57 - 1.75] (Hα | Hβ)	Yes
[O III] 4364*	4364.440	-	4356.4 – 4373.4	[0.57 - 1.75] (Hα | Hβ)	Yes
He I 4473*†	4472.760	-	4464.2 – 4481.2	[0.57 - 1.75] (Hα | Hβ)	No
[Fe III] 4659*†	4659.400	-	4652.7 – 4664.4	[0.57 - 1.75] (Hα | Hβ)	No
He II 4687	4687.015	-	4677.0 – 4697.0	[0.57 - 1.75] (Hα | Hβ)	Yes
[Ar IV] + He I 4713*†	4713.300	-	4852.7 – 4872.7	[0.57 - 1.75] (Hα | Hβ)	No
[Fe III] 4742*†	4741.500	-	4709.3 – 4717.3	[0.57 - 1.75] (Hα | Hβ)	No
Hβ	4862.683	-	4738.5 – 4744.5	[S III] 9533	Yes
[O III] 4960	4960.295	0.331 * OIII_5008	4919.0 – 4928.0	[O III] 5008	Yes
He I 4924*†	4923.500	-	4950.3 – 4970.3	[0.57 - 1.75] (Hα | Hβ)	No
[Fe III] 4988*†	4987.700	-	4984.0 – 4991.4	[0.57 - 1.75] (Hα | Hβ)	No
[O III] 5008	5008.240	-	4998.2 – 5018.2	[0.57 - 1.75] (Hα | Hβ)	Yes
[Fe II] 5018*†	5016.250	-	5012.6 – 5019.9	[0.57 - 1.75] (Hα | Hβ)	No
[N I] 5199†	5199.349	-	5189.3 – 5209.3	[0.57 - 1.75] (Hα | Hβ)	No
[N I] 5202†	5201.705	-	-1.0 – -1.0	[N I] 5199	No
[Fe VII] 5723*†	5723.200	-	5867.2 – 5887.2	[0.57 - 1.75] (Hα | Hβ)	No
[N II] 5757*†	5757.000	-	5715.7 – 5730.7	[0.57 - 1.75] (Hα | Hβ)	No
He I 5877	5877.252	-	5753.5 – 5760.5	[0.57 - 1.75] (Hα | Hβ)	Yes
[Fe VII] 6086*†	6086.000	-	6076.0 – 6096.0	[0.57 - 1.75] (Hα | Hβ)	No
[O I] 6302	6302.046	-	6296.0 – 6308.0	[0.57 - 1.75] (Hα | Hβ)	Yes
[S III] 6314*	6313.500	-	6309.5 – 6317.5	[0.57 - 1.75] (Hα | Hβ)	No
[O I] 6366	6365.536	0.32 * OI_6302	6355.5 – 6370.5	[O I] 6302	Yes

Continued on next page

[13] A | B denotes where the line is tied. Case A is redshifts less than z = 0.4963, Case B is for redshifts greater than z = 0.4963, [n-m] signifies the range multiplied by (A|B), in all cases the velocity is tied to be equal to the line that the dispersion is tied to

TABLE B1 – continued from previous page

[Fe X] 6374*†	6374.000	-	6370.0 – 6380.0	[0.57 - 1.75] (Hα | Hβ)	No
[N II] 6550	6549.860	0.326 * NII_6585	6542.9 – 6556.9	[N II] 6585	Yes
Hα	6564.608	-	6557.6 – 6571.6	[0.57 - 1.75] (Hα | Hβ)	Yes
[N II] 6585	6585.270	-	6575.3 – 6595.3	[0.57 - 1.75] (Hα | Hβ)	Yes
He I 6680*†	6679.750	-	6674.7 – 6684.7	[0.57 - 1.75] (Hα | Hβ)	No
[S II] 6718	6718.295	-	6711.3 – 6725.3	[0.57 - 1.75] (Hα | Hβ)	Yes
[S II] 6733	6732.674	-	6725.7 – 6739.7	[0.57 - 1.75] (Hα | Hβ)	Yes
He I 7068†	7067.657	-	7057.1 – 7077.1	[0.57 - 1.75] (Hα | Hβ)	No
[Ar III] 7138	7137.760	-	7127.8 – 7147.8	[0.57 - 1.75] (Hα | Hβ)	No
[O II] 7321*†	7321.200	-	7316.6 – 7325.8	[Ar III] 7138	No
[O II] 7332*†	7332.200	-	7327.4 – 7337.0	[0.57 - 1.75] (Hα | Hβ)	No
[Ar III] 7753†	7753.240	-	7743.2 – 7763.2	[0.57 - 1.75] (Hα | Hβ)	No
Pη†	9017.384	-	9007.4 – 9027.4	[0.57 - 1.75] (Hα | Hβ)	No
[S III] 9071†	9071.100	0.41 * SIII_9533	9061.1 – 9081.1	[S III] 9533	Yes
Pζ†	9231.546	-	9221.5 – 9241.5	[0.57 - 1.75] (Hα | Hβ)	No
[S III] 9533†	9533.200	-	9525.5 – 9540.9	[0.57 - 1.75] (Hα | Hβ)	Yes
Pϵ†	9548.588	-	9540.9 – 9556.3	[0.57 - 1.75] (Hα | Hβ)	No

C. CATALOG TABLES

Table C1: Emission Line Catalog Descriptions

Column Name	Unit	Format	Column Description
PMF_STRING	-	STRING	The combined Plate-MJD-Fiber of the spectrum
PLATE	-	STRING	The Plate
MJD	-	STRING	The Modified Julian Date of when the spectrum was taken
FIBER	-	STRING	The Fiber
Z	-	DOUBLE	The redshift
SC_VELOCITY	km s^{-1}	DOUBLE	The stellar continuum velocity as measured by the DAP
SC_VELOCITY_ERR	km s^{-1}	DOUBLE	The error in the stellar continuum velocity as measured by the DAP
SC_DISPERSION	km s^{-1}	DOUBLE	The intrinsic stellar continuum dispersion corrected for instrumental dispersion as measured by the DAP
SC_DISPERSION_ERR	km s^{-1}	DOUBLE	The error in the stellar continuum dispersion as measured by the DAP
SC_CORRECTION	km s^{-1}	DOUBLE	The stellar continuum correction applied to the SC_DISPERSION
SNR	-	DOUBLE	The median S/N ratio of spectrum
LINEID_FLUX	10^{-17} erg s^{-1} cm^{-2}	DOUBLE	The flux of a line given by LINEID as seen in Table B1
LINEID_FLUX_ERR	10^{-17} erg s^{-1} cm^{-2}	DOUBLE	The error in flux of a line given by LINEID as seen in Table B1
LINEID_EW	Å	DOUBLE	The restframe Gaussian equivalent width of a line given by LINEID as seen in Table B1
LINEID_EW_ERR	Å	DOUBLE	The error in the restframe Gaussian equivalent width of a line given by LINEID as seen in Table B1
LINEID_INT_EW	Å	DOUBLE	The restframe integrated equivalent width of a line given by LINEID as seen in Table B1
LINEID_INT_EW_ERR	Å	DOUBLE	The error in the restframe integrated equivalent width of a line given by LINEID as seen in Table B1
LINEID_SIGMA	km s^{-1}	DOUBLE	The intrinsic σ corrected for instrumental dispersion of a line given by LINEID as seen in Table B1
LINEID_SIGMA_ERR	km s^{-1}	DOUBLE	The error in σ of a line given by LINEID as seen in Table B1
LINEID_SIGMA_CORR	km s^{-1}	DOUBLE	The correction applied to the σ of a line given by LINEID as seen in Table B1

Table C2: Spectral Index Catalog Descriptions

Column Name	Format	Column Description
PMF_STRING	STRING	The combined Plate-MJD-Fiber
PLATE	STRING	The Plate
MJD	STRING	The Modified Julian Date
FIBER	STRING	The Fiber
Z	DOUBLE	The redshift
SNR	DOUBLE	The median S/N of spectrum
SPIND	DOUBLE	The value of the Spectral Index given by the Index column in Table 4 of K. B. Westfall et al. (2019)
SPIND_ERR	DOUBLE	The error in the Spectral Index given by the Index column in Table 4 of K. B. Westfall et al. (2019)

Table C3: AUXDATA Catalog Descriptions

Column Name	Format	Column Description
Template Weight Columns		
PMF_STRING	STRING	The combined Plate-MJD-Fiber
PLATE	INT	The Plate
MJD	INT	The Modified Julian Date
FIBER	INT	The Fiber
E(B-V)	DOUBLE	The E(B-V) of the Milky Way at the position of the spectrum used as input to the eBOSS-DAP, see Step **(2)** in §3.3
RCHI2	DOUBLE	The reduced χ^2 of the best-fit stellar continuum model
FIBERMASKED	BOOLEAN	Flag for spectra masked with a full fiber mask (T for masked, F for unmasked), see §3.2.1
AgeXX_XXXXMetY_Y	DOUBLE	Weight given to the SSP template with age XX.XXXX Gyr and metallicity Y.Y $Z_\odot$
AgeC_XXXXMetY_Y+nebcont	DOUBLE	Weight given to the continuous template with age 0.XXXX Gyr and metallicity Y.Y $Z_\odot$, including nebular continuum emission
multicoeff_N	DOUBLE	Polynomial coefficient of order N, in units identical to the spectrum
Photometric & Spectrophotometric Quantities (from spAll[a])		
SPECPRIMARY	BYTE	Flag set to 1 for the primary observation among repeat/duplicate spectra of the same object; use to remove duplicates
SN_MEDIAN_G	FLOAT	Median S/N per pixel in the g band
SN_MEDIAN_R	FLOAT	Median S/N per pixel in the r band
SN_MEDIAN_I	FLOAT	Median S/N per pixel in the i band
SN_MEDIAN_ALL	FLOAT	Median S/N per pixel across all bands
MODELFLUX_G	FLOAT	Best-fit model flux in the g band
MODELFLUX_R	FLOAT	Best-fit model flux in the r band
MODELFLUX_I	FLOAT	Best-fit model flux in the i band
MODELFLUX_IVAR_G	FLOAT	Inverse variance of MODELFLUX_G
MODELFLUX_IVAR_R	FLOAT	Inverse variance of MODELFLUX_R
MODELFLUX_IVAR_I	FLOAT	Inverse variance of MODELFLUX_I
SPECTROFLUX_G	FLOAT	Spectroscopic flux in the g band
SPECTROFLUX_R	FLOAT	Spectroscopic flux in the r band
SPECTROFLUX_I	FLOAT	Spectroscopic flux in the i band
PETROTH90_I	FLOAT	Petrosian 90% light radius in the i band (arcsec)
PETROTH90ERR_I	FLOAT	Uncertainty on PETROTH90_I (arcsec)
LAMBDA_EFF	FLOAT	Effective wavelength of the fiber offset correction (Å)
RA	DOUBLE	Right Ascension (J2000, degrees)
DEC	DOUBLE	Declination (J2000, degrees)
spZline Emission-Line Fluxes[b]		
SPZ_OII_3727_FLUX	FLOAT	[O II] 3727 flux (10^{-17} erg s^{-1} cm^{-2})
SPZ_H_beta_FLUX	FLOAT	Hβ flux (10^{-17} erg s^{-1} cm^{-2})
SPZ_OIII_5007_FLUX	FLOAT	[O III] 5007 flux (10^{-17} erg s^{-1} cm^{-2})
SPZ_H_alpha_FLUX	FLOAT	Hα flux (10^{-17} erg s^{-1} cm^{-2})
SPZ_NII_6584_FLUX	FLOAT	[N II] 6584 flux (10^{-17} erg s^{-1} cm^{-2})
SPZ_SII_6717_FLUX	FLOAT	[S II] 6717 flux (10^{-17} erg s^{-1} cm^{-2})
SPZ_SII_6731_FLUX	FLOAT	[S II] 6731 flux (10^{-17} erg s^{-1} cm^{-2})
Target Classification & Fiber Aperture		
INFIBER	FLOAT	Fraction of galaxy light within the 2″ fiber aperture (i band)
INFIBER_SN	FLOAT	Signal to noise of INFIBER
TARGET_TEXT	STRING	Full SDSS target type string
TARGET_CLASS	STRING	Target class (QSO, LRG3, LRG4, LRGL, ELG, TDSP, ANCI, MISC); see Table A1

[a] https://data.sdss.org/datamodel/files/BOSS_SPECTRO_REDUX/RUN2D/spAll.html
[b] https://data.sdss.org/datamodel/files/SPECTRO_REDUX/RUN2D/PLATE4/spZline.html

D. ADDITIONAL SPECTRUM FIT PLOTS

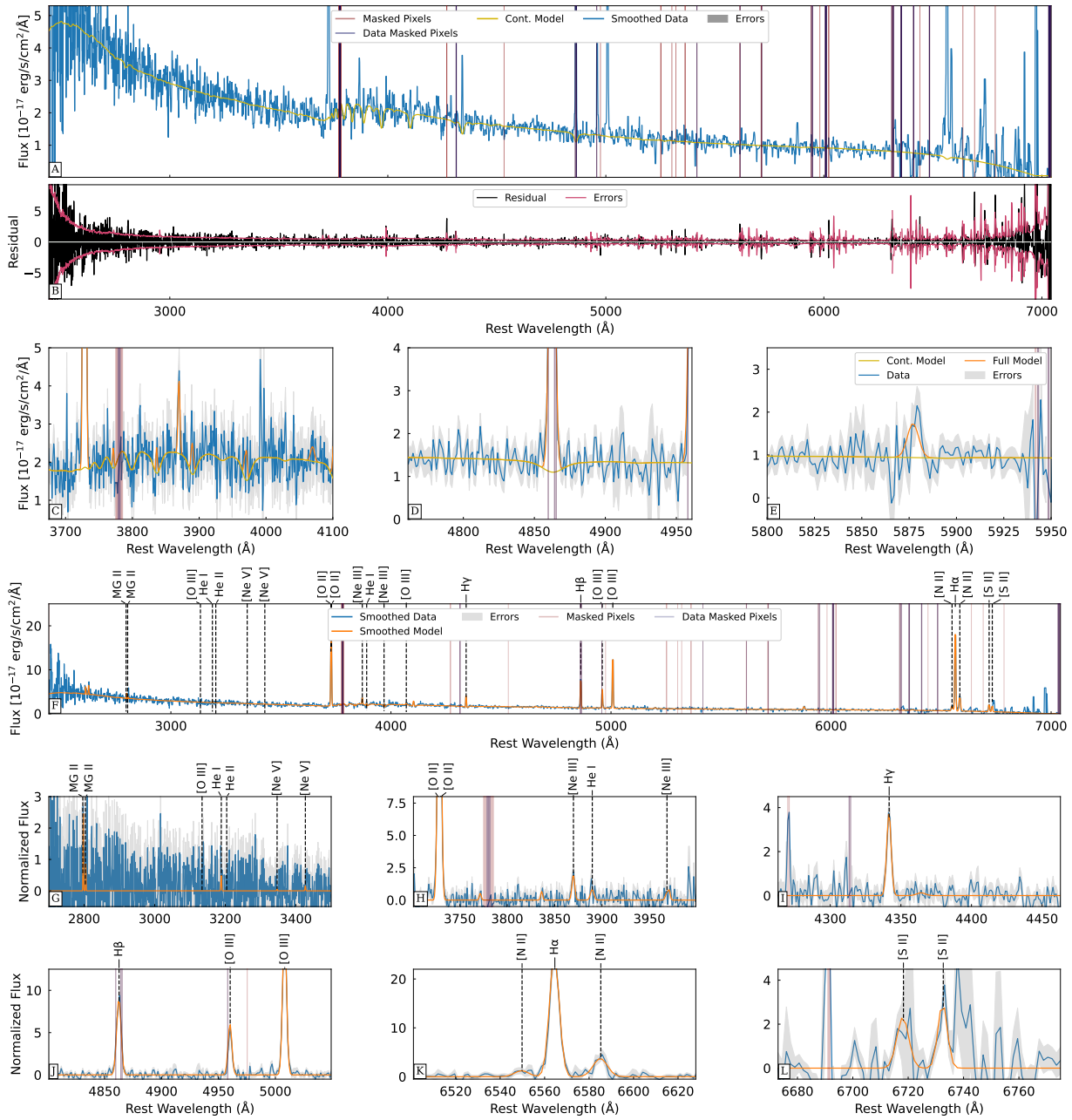


Figure D1. Sample star-forming galaxy fit for the spectra spec-7386-56769-0560.fits, which was categorized as an SFG using the BPT AGN Diagnostic. All plotting information is identical to figure 12.

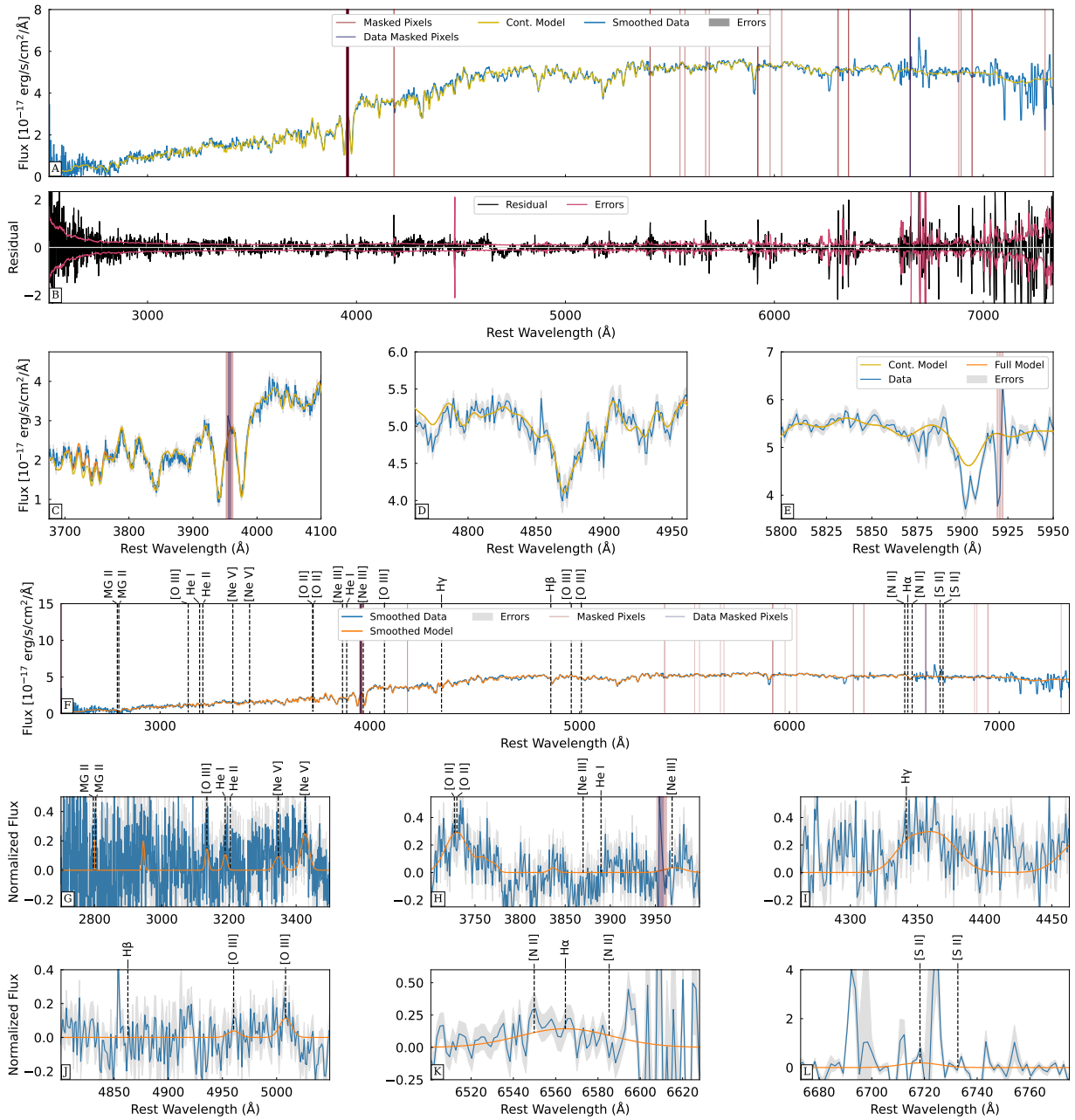


Figure D2. Sample galaxy fit plots for the spectra spec-6138-56598-0432.fits, which we classified as a red dead galaxy. All plotting information is identical to figure 12.

E. SURVEY CHOICE ERROR ANALYSIS PLOTS

To evaluate the impact of the EW-based line-set division and the redshift-based anchor-line change on the consistency of our emission–line measurements, we selected a random subsample of 4171 spectra satisfying $9 < \mathrm{EW}_{\mathrm{H}\beta} < 11$ Å and $0.1 < z < 0.4$, ensuring that all objects lie near the equivalent–width boundary while retaining all relevant lines within a regime of low spectrophotometric error. In all comparisons below, we compute symmetric percent differences and normalize by the propagated measurement error using only those emission lines detected at S/N > 3.

We first assess the effect of the EW division by refitting the spectra in our comparison sample under two different modeling choices: one using the full set of 80 emission lines and one using the reduced set of 27 lines. For this analysis, we use Hβ as the tying line since this configuration is used for 61% of the eBOSS–DAP catalog. Because the underlying galaxy sample is identical in both cases, any differences in the recovered fluxes directly reflect the impact of the emission line set used. Across the six prominent lines considered ([O II] 3727+3729, Hβ, [O III] 5008, Hα, [N II] 6585, and [S II] 6718+6733), the mean percent difference between the full and reduced line-set fits is consistent with zero for all six lines, with the largest offset being 0.7% for [N II] 6585. The mean difference normalized by the propagated measurement error is also small for all lines, reaching at most ∼8% of the measurement error for Hβ. We therefore find no systematic offset introduced by the choice of line list; any differences between the full and reduced line sets are consistent with random measurement noise. Exact values for each line are given in Table E1. As illustrated in Figure E1, the flux ratios show negligible systematic trend with S/N above S/N > 3, confirming that the choice between the full and reduced line sets has no significant effect on the recovered fluxes.

We next assess the effect of the reference line change by taking the same set of spectra and refitting them with the reduced set of emission lines, tying all kinematics to Hα instead of Hβ. We then compare the emission line fluxes measured with the 27-line list using different reference lines (Hα or Hβ) to isolate the impact of the reference line choice. Across the same six emission lines, the mean percent difference between the Hα-tied and Hβ-tied fits is consistent with zero for all six lines, with the largest offset being 0.4% for [N II] 6585. The mean difference normalized by the propagated measurement error is also small for all lines, reaching at most ∼3% of the measurement error for Hβ. We therefore find no systematic offset introduced by the choice of reference line; any differences between the Hα-tied and Hβ-tied fits are consistent with random measurement noise. Exact values for each line are given in Table E2. As shown in Figure E2, the flux ratios remain tightly clustered with no significant trend with S/N, indicating that the choice of tying line has no meaningful effect on the recovered fluxes.

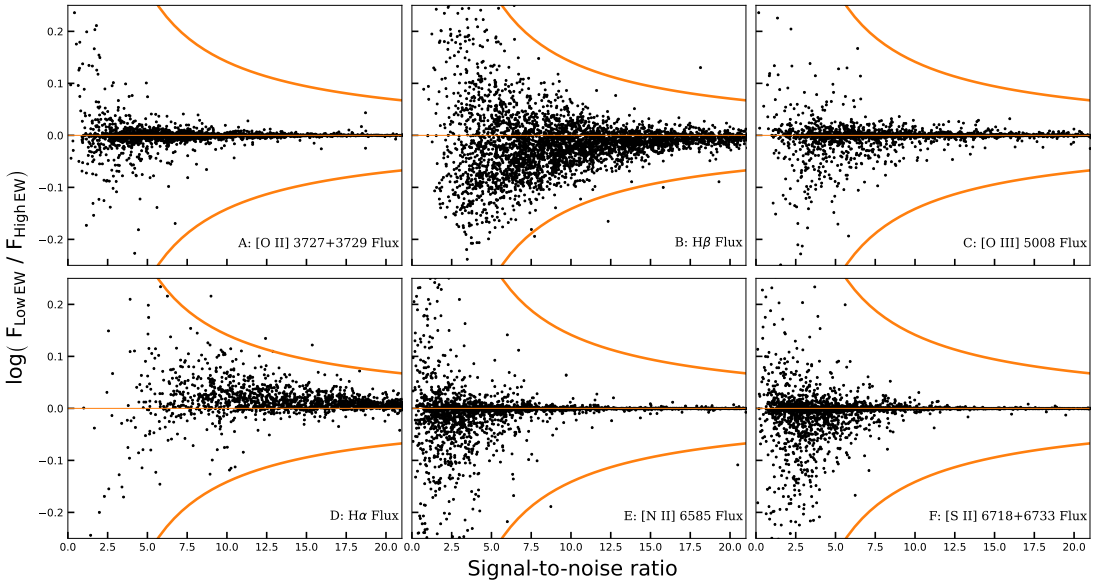


Figure E1. Comparison of line flux measurements obtained by running the eBOSS–DAP on a random subsample of 4171 spectra satisfying $9 < \mathrm{EW}_{\mathrm{H}\beta} < 11$ Å and $0.1 < z < 0.4$, fit using Hβ as the tying line. For each of the six strong emission lines, the y-axis shows $\log(\mathrm{F}_{\mathrm{Low\,EW}}/\mathrm{F}_{\mathrm{High\,EW}})$, where $\mathrm{F}_{\mathrm{Low\,EW}}$ is the flux measured using the reduced 27–line set and $\mathrm{F}_{\mathrm{High\,EW}}$ is the flux measured using the full 80–line set for the identical object and line. The x-axis shows the signal–to–noise ratio of that line measured in the full 80–line set. The orange lines show the expected 1σ flux uncertainties as a function of S/N. The data points do not show a significant systematic offset and they lie well inside the orange lines, indicating that the difference induced by our choice of line list is significantly smaller than the random error.

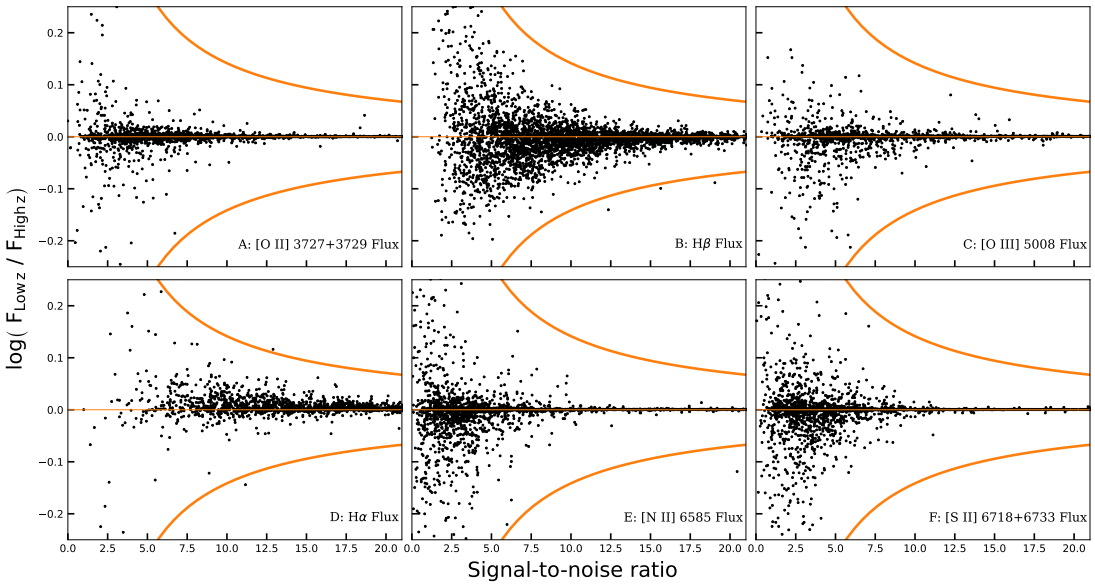


Figure E2. Comparison of line–flux measurements obtained by running the eBOSS–DAP on the same random subsample of 4171 spectra satisfying $9 < \mathrm{EW}_{\mathrm{H}\beta} < 11$ Å and $0.1 < z < 0.4$, using the two line–tying prescriptions employed in the eBOSS–DAP: tying all kinematics to Hα for $z < 0.4963$ and tying all kinematics to Hβ for $z > 0.4963$. For each of the six strong emission lines, the y-axis shows $\log\left(\mathrm{F}_{\mathrm{Low\,z}}/\mathrm{F}_{\mathrm{High\,z}}\right)$, where $\mathrm{F}_{\mathrm{Low\,z}}$ is the flux measured using the Hα tying configuration (low–z prescription) and $\mathrm{F}_{\mathrm{High\,z}}$ is the flux measured using the Hβ tying configuration (high–z prescription) for the identical object and line. The x-axis shows the signal–to–noise ratio of that line measured using the Hβ tying configuration. The orange curves show the expected 1σ flux uncertainties as a function of S/N. The data points do not show a significant systematic offset and they lie well inside the orange lines, indicating that the difference induced by our choice of anchor line is significantly smaller than the random error.

Table E1: Comparison of Emission-Line Fluxes: High-EW vs. Low-EW Line List (High-z, Hβ-tied)

Line	N_{gal}	Mean % Diff	Std % Diff	Mean σ-ratio
[O II] 3727+3729 Flux	4144	0.01	6.69	0.0016
Hβ Flux	4067	0.99	6.69	0.0849
[O III] 5008 Flux	3974	0.23	3.97	0.0067
Hα Flux	4166	-0.55	3.44	-0.0682
[N II] 6585 Flux	4080	0.74	14.08	0.0153
[S II] 6718+6733 Flux	4111	0.71	7.39	0.0136

Note. — Mean % Diff is the per-galaxy percent difference $(F_1 - F_2)/((F_1 + F_2)/2) \times 100$, averaged over the sample; values far from 0 indicate a systematic offset between the two configurations. Std % Diff is the scatter in that per-galaxy percent difference (random variation). Mean σ-ratio is the mean percent difference normalized by the propagated measurement error; values near 0 indicate the offset is consistent with measurement noise alone.

Table E2: Comparison of Emission-Line Fluxes: Hα-Tied vs. Hβ-Tied (Low-EW, Low-z)

Line	N_{gal}	Mean % Diff	Std % Diff	Mean σ-ratio
[O II] 3727+3729 Flux	3998	-0.19	7.00	0.0008
Hβ Flux	4024	0.12	5.13	0.0251
[O III] 5008 Flux	3996	0.33	4.10	0.0085
Hα Flux	4021	-0.22	3.10	-0.0288
[N II] 6585 Flux	3929	0.35	15.40	0.0106
[S II] 6718+6733 Flux	3966	0.39	8.34	0.0082

Note. — See Table E1 for column definitions.

F. Hβ vs. stellar continuum velocity dispersion

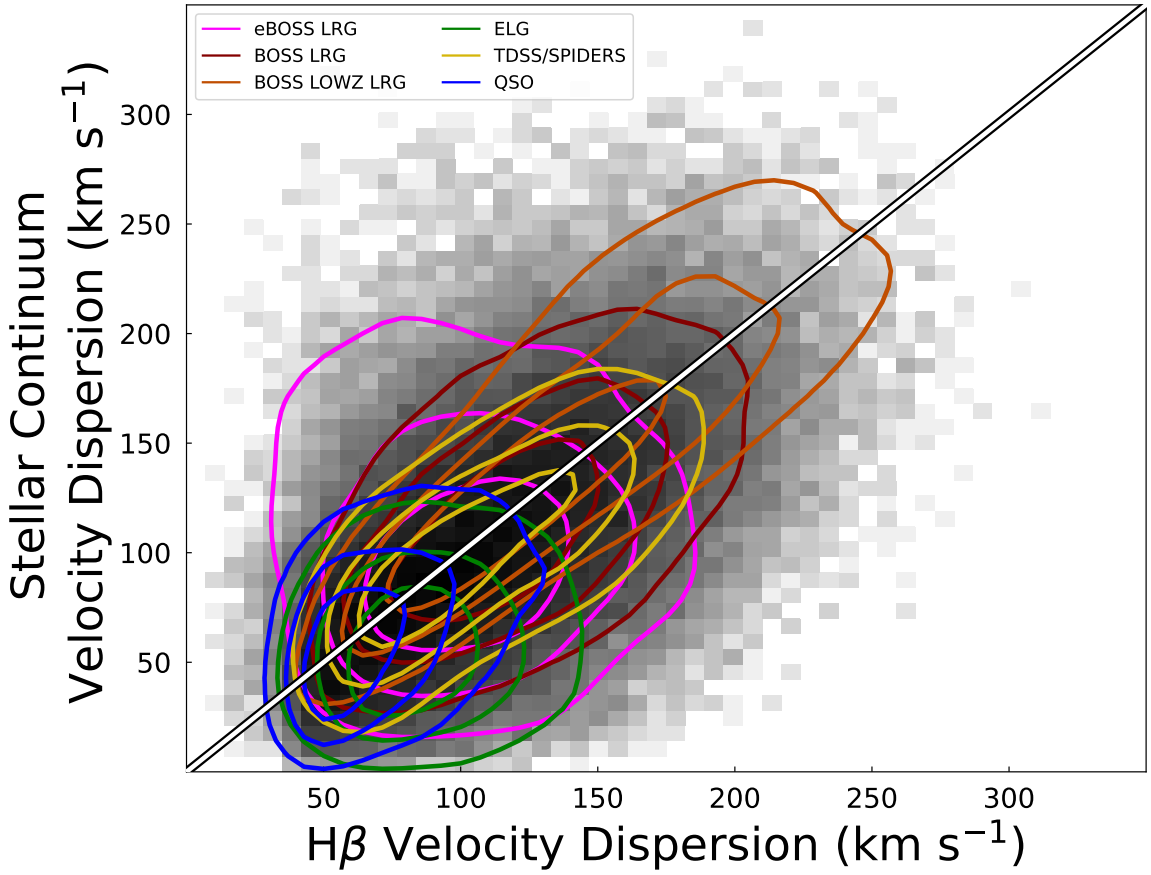


Figure F1. Hβ emission-line velocity dispersion vs. stellar continuum velocity dispersion for eBOSS galaxies with stellar continuum dispersion error < 50 km s^{-1}, Hβ dispersion error < 50 km s^{-1}, Hβ S/N > 3, and Hβ EW > 3 Å. The grayscale is a 2D log-scaled histogram of the full sample. The contours show the different target classes; the outermost contour for each class encloses 75% of the total sample. The one-to-one line is shown in white. The strong agreement between the two independent dispersion measurements across most target classes confirms that the stellar continuum velocity dispersions measured by the eBOSS-DAP are reliable. The one exception is the ELGs, which have stellar velocity dispersions that are 25 km s^{-1} lower than their gas dispersion, on average. This offset may be due to physical effects (e.g., the gas tracing more of the galaxy's rotation curve than the starlight).

This paper was built using the Open Journal of Astrophysics LaTeX template. The OJA is a journal which provides fast and easy peer review for new papers in the `astro-ph` section of the arXiv, making the reviewing process simpler for authors and referees alike. Learn more at http://astro.theoj.org.